

## **Final Technical Report**

External Grant Award Number:  
**08HQGR0046**

Recipient:  
**Board of Regents of the Nevada System of Higher Education  
on Behalf of  
The University of Nevada, Reno**

Principal Investigators:  
**John N. Louie**  
Telephone: (775) 784-4219 Fax: (775) 784-4165 louie@seismo.unr.edu  
<http://www.seismo.unr.edu/wbrcvm>  
**Leiph Preston**  
Telephone: (505) 284-7672 Fax: (505) 844-7354 lpresto@sandia.gov  
**Ileana M. Tibuleac**  
Telephone: (775) 784-6256 Fax: (775) 784-4165 ileana@seismo.unr.edu

Title:  
**Basin Model Improvements and Verification for Reno Area  
3-D Scenario Modeling**

**NEHRP Element(s):**  
ELEMENT I: National and regional earthquake hazards assessments.  
**Keywords:** Site effects, Basin effects, Scenario modeling, Ground motions,  
Seismic zonation, Engineering seismology

Research supported by the U.S. Geological Survey (USGS), Department of the Interior, under USGS award number **08HQGR0046**. The views and conclusions contained in this document are those of the authors and should not be interpreted as necessarily representing the official policies, either expressed or implied, of the U.S. Government.

External Grant Award Number **08HQGR0046**

## **Basin Model Improvements and Verification for Reno Area 3-D Scenario Modeling**

**John N. Louie and Ileana M. Tibuleac**

University of Nevada Seismological Laboratory, Reno, NV 89557  
Telephone: (775) 784-4219 Fax: (775) 784-4165 [louie@seismo.unr.edu](mailto:louie@seismo.unr.edu)  
<http://www.seismo.unr.edu/wbrcvm>

**Leiph Preston**

Sandia National Laboratories<sup>1</sup>, Albuquerque, NM, 87185-0750

### **NON-TECHNICAL ABSTRACT**

The USGS has been conducting research into physics-based modeling of shaking from scenario earthquakes for Seattle and Salt Lake City, in concert with similar efforts for northern and southern California. Since the USGS-NEHRP program has construction of new earthquake-hazard maps for Reno as a top regional priority, they have generously funded new research to start up a physics-based shaking-prediction effort for Nevada. Such scenario modeling requires assembling available geological, geophysical, and geotechnical results for the region into a Community Velocity Model or “CVM,” and validating intensive CVM computational results against recorded shaking data. Technical details are at [www.seismo.unr.edu/wbrcvm](http://www.seismo.unr.edu/wbrcvm). This project succeeded in its efforts to combine all the latest geological and geophysical knowledge of the Reno area into a coherent model, and tested that model against earthquake recordings including several made during the Mogul/West Reno earthquake swarm in early 2008. The tests revealed that our knowledge of the local basin structure is still incomplete, motivating additional and ongoing studies targeted at the features we find most inconsistent with prior knowledge. Among these studies is research into a brand-new method of probing basin structure, developed under this project at the Univ. of Nevada, that uses ambient ground noise recorded at local earthquake-location stations.

---

<sup>1</sup> Sandia National Laboratories is a multi-program laboratory operated by Sandia Corporation, a wholly owned subsidiary of Lockheed Martin company, for the U.S. Department of Energy’s National Nuclear Security Administration under contract DE-AC04-94AL85000. Approved for public release; further dissemination unlimited.

External Grant Award Number **08HQGR0046**

## **Basin Model Improvements and Verification for Reno Area 3-D Scenario Modeling**

**John N. Louie and Ileana M. Tibuleac**

University of Nevada Seismological Laboratory, Reno, NV 89557  
Telephone: (775) 784-4219 Fax: (775) 784-4165 [louie@seismo.unr.edu](mailto:louie@seismo.unr.edu)  
<http://www.seismo.unr.edu/wbrcvm>

**Leiph Preston**

Sandia National Laboratories, Albuquerque, NM, 87185-0750

### **TECHNICAL ABSTRACT**

An accurate understanding of earthquake ground motions and their variability in the Reno and Carson City region is important to realistically quantify seismic hazard. Geologic evidence indicates the potential for large magnitude (M7-7.5) events occurring on local faults, such as the Genoa Fault, which could pose a severe risk to lives and property in this growing metropolitan area. Despite the wealth of data from the 2008 Mogul/West Reno earthquake swarm, we must rely on 3-D scenario modeling to estimate ground motions from expected damaging earthquakes. In constructing a realistic scenario for the Reno-Carson City region, we first needed accurate estimates of the structure and velocities of the basins where the cities lie. Our primary goal was to construct and validate a realistic velocity-structure model in the Reno-Carson City region. Prior NEHRP-funded research provided the necessary background 3-D velocity model of the entire region down to several kilometers depth. We added higher-resolution structural information in the populated Reno basin to achieve more realistic scenarios. We supplemented the regional 3-D velocity model with high-resolution velocities obtained by cross-correlating seismic noise between the densely spaced stations in the basins of Reno and Carson City, a new technique developed for this project that should find wide application. Additionally, very high-resolution Vs30 measurements previously acquired in Reno were included in our community velocity model. We conducted validation on the model by comparing waveforms from earthquakes recorded on the network against E3D finite-difference scenario calculations of these earthquakes. Validation used four models; consisting of CVMs with and without tomography results, each with and without topography. Unfortunately, there is no clearly better model that works for all events and for all stations. There are instances where any of the four synthetic models match the observations better than any of the others. However, none of the models provide excellent fit to the observed waveforms. Only qualitative measures of fit can be used due to these deficiencies. Near-offset receivers tend to show the best fit to observations, but in these cases, all four models can fit the data almost equally well. With these caveats, however, the new CVM with topography tends to produce the best fit to the observations. But it is only marginally better than the others. This result points to further fundamental deficiencies in our knowledge of the structure of the Reno-area basin, which we hope to resolve in future work.

External Grant Award Number **08HQGR0046**

## **Basin Model Improvements and Verification for Reno Area 3-D Scenario Modeling**

**John N. Louie and Ileana M. Tibuleac**

University of Nevada Seismological Laboratory, Reno, NV 89557  
Telephone: (775) 784-4219 Fax: (775) 784-4165 [louie@seismo.unr.edu](mailto:louie@seismo.unr.edu)  
<http://www.seismo.unr.edu/wbrcvm>

**Leiph Preston**

Sandia National Laboratories, Albuquerque, NM, 87185-0750

### **NEHRP Element(s):**

ELEMENT I: National and regional earthquake hazards assessments.

**Keywords:** Site effects, Basin effects, Scenario modeling, Ground motions,  
Seismic zonation, Engineering seismology

### **Introduction**

An accurate understanding of the ground motions and their variability in the Reno-Carson City region from earthquakes is important to realistically quantify seismic hazard. Geologic evidence indicates the potential for large magnitude (M7-7.5) events occurring on local faults, such as the Genoa Fault, which could pose a severe risk to lives and property in this growing metropolitan area (e.g., dePolo et al., 1997). Fortunately, no large earthquakes have struck the region since it has become heavily populated. The Mogul/West Reno earthquake swarm of 2008 actually provided a few strong-motion records in limited areas of the city (Anderson et al., 2009), and vastly increased the number of records available from the urban basin. But the paucity of records from events outside the Mogul source still precludes a precise knowledge of expected ground motions from the most probable damaging events. Thus, we must rely on scenario modeling to estimate ground motions from expected damaging earthquakes.

We initiated construction of realistic ground motion scenarios for the Reno-Carson City urban corridor, requiring 1) knowledge of the high-resolution velocity structure of the surrounding region, 2) understanding of the effects of topography on site amplification and 3) validation of synthetic waveforms with observed waveforms. The first two requirements are fundamental to computing the most accurate waveforms and the last is necessary for evaluating whether our knowledge of the earth, in conjunction with the abilities of the synthetic waveform computation code, is sufficient to provide realistic input to hazard analyses.

The primary goal of this research was to construct an improved 3-D velocity model of the region and to validate this model using previously recorded earthquakes. The improved 3-D velocity model required collation of data sets of various resolutions into one community velocity model. Existing data sets such as the previously NEHRP-funded regional 3-D velocity model, Vs30 measurements, and structural estimates from gravity in the basins were combined with newer data to form a single unified model. The appendix describes a new high-resolution basin velocity model derived from seismic noise cross-correlation between the densely spaced stations within the Reno and Carson City area basins. Secondly, we validated this community velocity model using the E3D finite-difference 3-D elastic waveform calculation code (Graves, 1996) to

compute earthquake ground motion scenarios for previously recorded events in the Reno-Carson City region. The validation testing allowed us to determine which areas of the model most need further research. The validated community velocity model will be helpful in completing future scenario modeling studies.

This work directly addressed Element I of U.S. Geological Survey's Earthquake Hazards Program (EHP) as "research that contributes to improvements in the national hazards maps and to assessing earthquake hazards and reducing losses in urban areas," and Element III by investigating possible ground-shaking effects in the Reno urban area. "Priority Topics in Research on Earthquake Effects" that this project addressed included seismogram synthesis for "3D basin effects," "Improve observations relevant to the shaking behavior of near-surface materials in high-risk urban areas," and "Improve site characterization for building code and other applications."

The project also met a goal stated in the "Priorities in the National/Intermountain West (NIW)" Nevada section, among which are to "improve and validate 3D velocity models needed for waveform modeling of the effects of basin- and near-surface-geology for Reno-Carson City, ... and incorporate results into the Community Velocity Model." One result of this project is a complete community velocity model for the Reno/Carson region, available to all interested researchers through [www.seismo.unr.edu/wbrcvm](http://www.seismo.unr.edu/wbrcvm).

By improving our understanding of expected ground motions, our results will directly apply to reducing losses from earthquakes in Reno. Reno is particularly important as a rapidly growing community, in a location where the seismic hazard is known to be high.

## **Methods and Results**

### **Velocities**

Until recently the regional seismic velocity structure (on the scale of a few km resolution) was largely unknown in the Reno-Carson City area. However, a previous NEHRP project by von Seggern and Preston to study the 3-D P- and S-wave velocity structure under this growing metropolitan area has recently been completed (Preston and von Seggern, 2007). The results of this study provide a comprehensive image of the regional velocity structures primarily between 2 and 20 km depth. Knowledge of the 3-D velocity structure to these depths is critical to proper computation of wavefields from more distant sources to the urban basins in the region, such as an event on the southern Genoa fault system to the Reno basin. Although velocities are best imaged below ~2 km depth, the overall structure of basins where ANSS station coverage is good was resolved. Besides the Reno basin, these include the relatively poorly studied basins such as Washoe Valley, Eagle Valley (Carson City), and Carson Valley. These velocity models were integrated into the community velocity model that we constructed as part of this effort. Preliminary results of the P-wave tomography are shown in figure 1.

Trial computations for the Las Vegas basin by Louie et al. (2006) have suggested that a model with pervasive lateral heterogeneity at the surface can trap additional energy, even at a relatively low frequency of 0.5 Hz. The scattering and lensing leads to amplification, over a model with a laterally homogeneous basin surface zone, of several times the 20% variability in zone velocity. For this reason we felt that it was important to test model grids that respect the variations in Vs30 and Vs100 measured within the Reno basin. We took advantage of site-condition measurements collected recently at most ANSS stations in Reno by Pancha et al. (2007), and across the Reno basin by Scott et al. (2004). These measurements yielded depth-averaged shear velocity values to 100 m depths (Vs100) as well as Vs30 values (fig. 2). Figure 2



also shows basin depth as derived from the gravity results of Abbott and Louie (2000), improved in West Reno by gravity studies conducted by the Washoe County Dept. of Water Resources (Widmer et al., 2007).

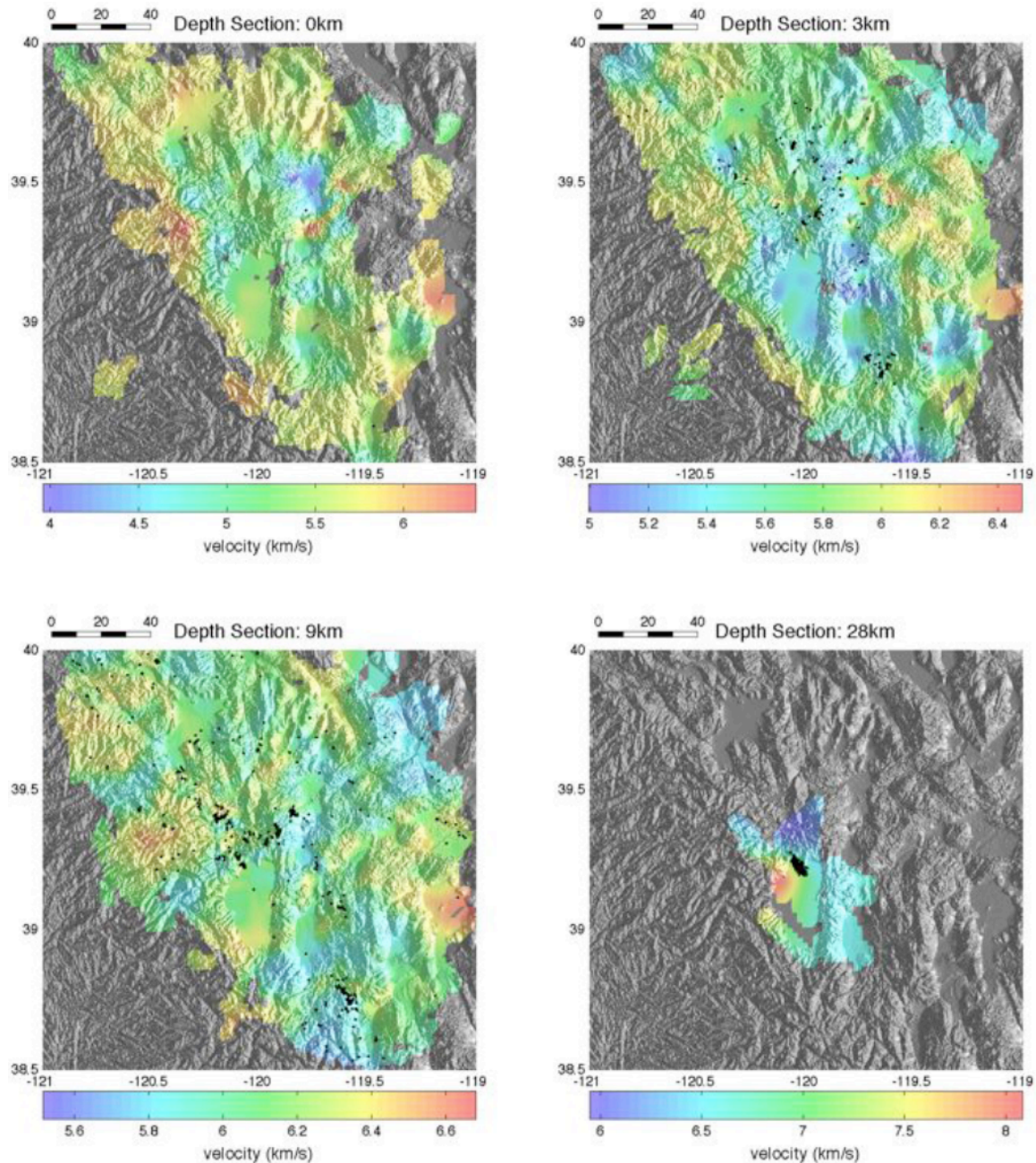


Figure 1: Vp depth maps over shaded relief, from the regional tomography results of Preston and von Seggern (2007). Grey regions indicate no ray coverage. Black dots are relocated seismicity within  $\pm 1$  km of the given depth section.

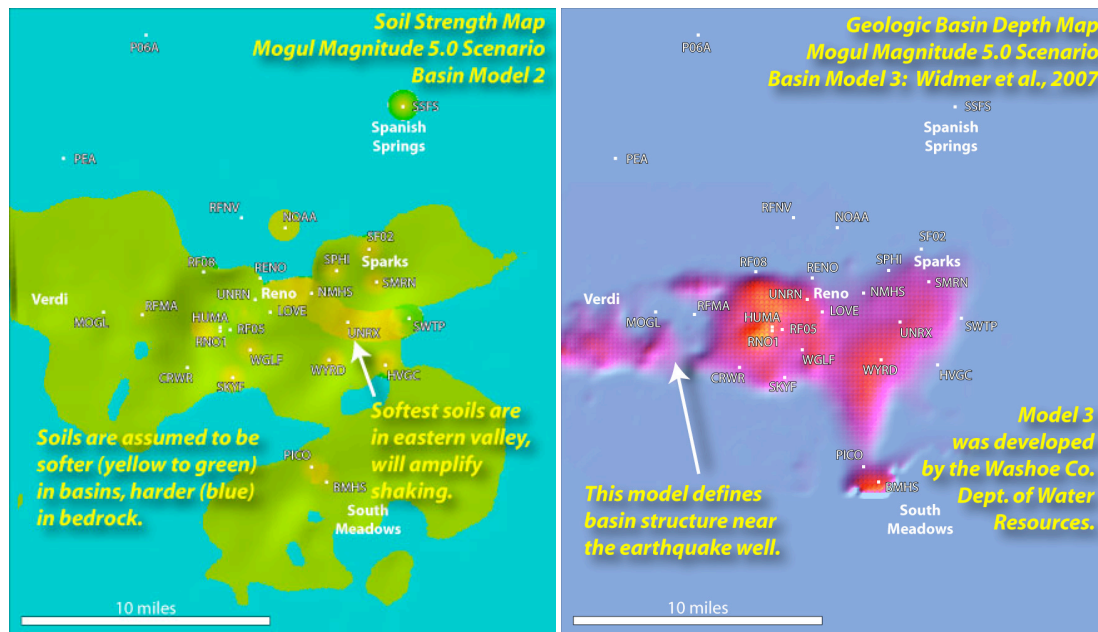


Figure 2: (left) Vs30 map of the Reno-area urban basin, combining the transect measurements of Scott et al. (2004) with the ANSS station measurements of Pancha et al. (2007), with the Abbott and Louie (2000) basin model in shaded relief. Yellow color indicates Vs30 at the NEHRP C-D boundary, 360 m/s, and the green-cyan boundary is the at the B-C boundary, 760 m/s. (right) The new Reno-area basin thickness model of Widmer et al. (2007), with 1-km maximum thicknesses yellow, zero thickness blue.

Combining all of the above velocity information into a single unified community velocity model was not a trivial task. The various sources of velocity information had a wide range of resolutions and coverages. Fortunately, the open-source ModelAssembler package that has been developed at NSL allows the construction of a single unified velocity model from such disparate model sources. Rules controlled by the user can be applied to combine, smoothly stitch, and weight the various models. These parameters must be evaluated to determine the optimum combination consistent with the resolution, coverage, and limitations of each data set. For example, where higher resolution basin data exist, such as in the Reno basin, these data should be given preference over the lower resolution regional tomography, although they must be combined in such a way that is consistent with the regional tomography. It was particularly important that interpolation of Vp or Vs individually not drive the Vp/Vs ratio to absurd values. The experience of our team combined with the capabilities of the ModelAssembler code was essential to producing a self-consistent, unified community velocity model. The code and the model are available at [www.seismo.unr.edu/ma](http://www.seismo.unr.edu/ma). Figure 3 shows cross sections of the new, integrated model.

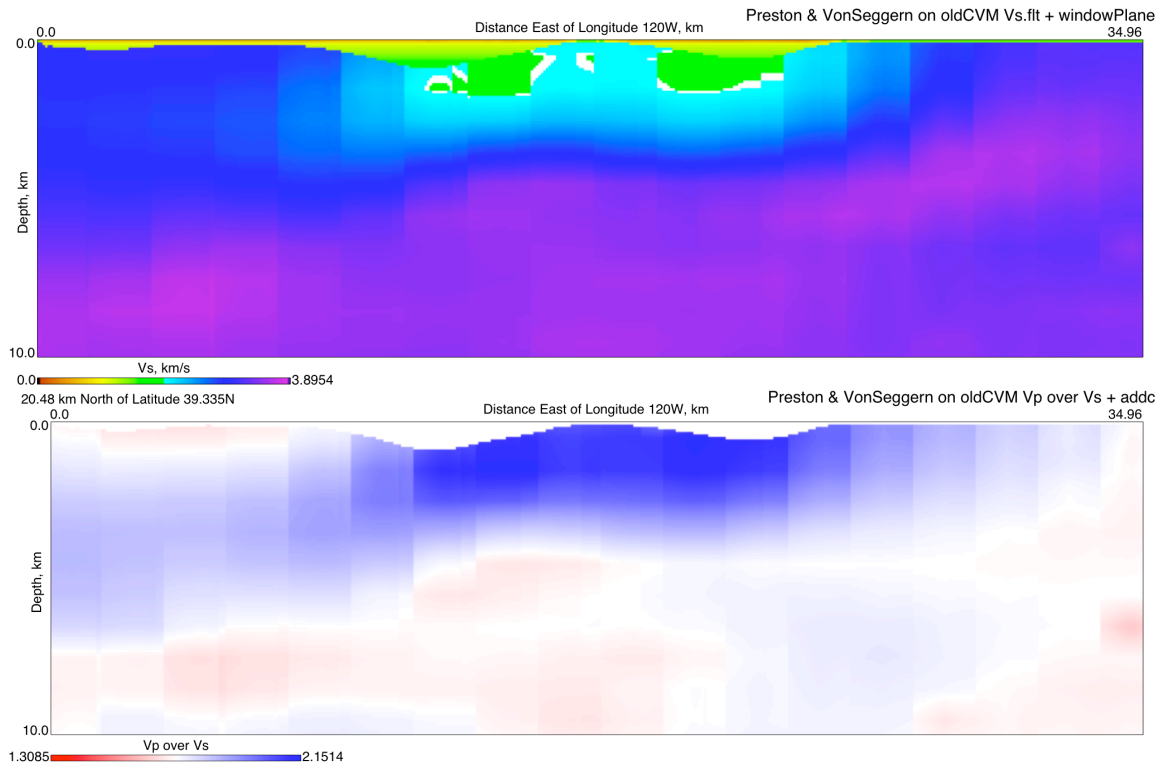


Figure 3: (top) West-east shear-velocity section across the deepest portion the Reno-area urban basin, combining the Abbott and Louie (2000) basin model with the regional tomography of Preston and von Seggern (2007), with the geotechnical layer affecting the surface zone— here with no topography. (bottom) Section checking the resulting Vp/Vs ratio after combination, showing that combined-model Vp/Vs does not exceed the 2.15 maximum value found in the tomography.

## Full waveform simulation procedure

The community velocity models (CVM) are constructed without reference to topography. As such, when simulating the no topography cases, the models are used without alteration. When topography is used, however, the models are adjusted to conform to the topographic surface. The zero depth layer of the original CVM is assumed to correspond to the topographic surface. Thus, for each (x,y) position in the CVM, the entire column (in z) is adjusted downward so that the zero depth position will lie at the topographic surface (Figure 4). Nodes above the topographic surface are filled with the value of the nodes in the same column at the topographic surface. Values that would extend below the maximum depth of the model are discarded. Additionally, a 5 node “buffer” zone is created in all three dimensions where the value at 5 nodes in from the edge of the model is used to fill this zone. This is necessary to avoid an instability in E3D that was discovered during initial simulations, most likely due to the Clayton-Engquist (Clayton and Engquist, 1977) boundary conditions that are used for the simulations. E3D uses the density extinguishing approach (Schultz, 1997) in order to simulate the effects of topography.

The models used for E3D use the same dimensions and node spacing as the original CVM, i.e.  $n_x=437$ ,  $n_y=499$ ,  $n_z=125$ ,  $dh=80$  m where x runs east-west, y runs north-south, z increases with depth and dh is the node spacing in all 3 dimensions. The origin of the model is located in the southwest corner at  $120.0^\circ$  W longitude and  $39.335^\circ$  N latitude. The simulation time step is 6 ms for the old CVM and 5 ms for the new CVM. This difference is necessitated



due to higher velocities present in the new CVM compared with the old. The total simulation time is 60 s for both models. Both models and all events use a gaussian source-time function with a full-width at half-max of 1 s (Figure 5). Attenuation, which is part of the CVMs based on the Q-to-velocity relations of Olsen et al. (2003), was utilized in the simulations.

A total of six events are simulated as indicated in the table below and Figure 6. Event depths are relative to the zero-depth layer of the original CVM in the no topography cases and are adjusted by the same vertical distances as the model parameters in the topographic cases. Twenty-seven three-component stations are utilized and correspond to actual stations locations. Stations are located at the zero-depth layer (free surface) in the no topography cases and at their appropriate elevations in the topographic cases (Figure 6).

<b><i>Event</i></b>	<b><i>Origin Time (UT)</i></b>	<b><i>Latitude (N)</i></b>	<b><i>Longitude (W)</i></b>	<b><i>Depth (km)</i></b>	<b><i>Mag</i></b>
1	4/26/2008 6:40:10.6	39.5197	119.9303	1.4	4.7
2	6/12/2006 13:52:16.6	39.4327	119.7516	8.3	2.7
3	6/08/2008 17:53:40.6	39.5495	119.9124	2.6	3.6
4	5/03/2007 15:34:06.5	39.4160	119.9416	9.2	1.8
5	8/05/2008 21:59:39.3	39.5615	119.9565	6.6	2.8
6	5/06/2008 8:41:44.2	39.4853	119.8848	3.2	2.5

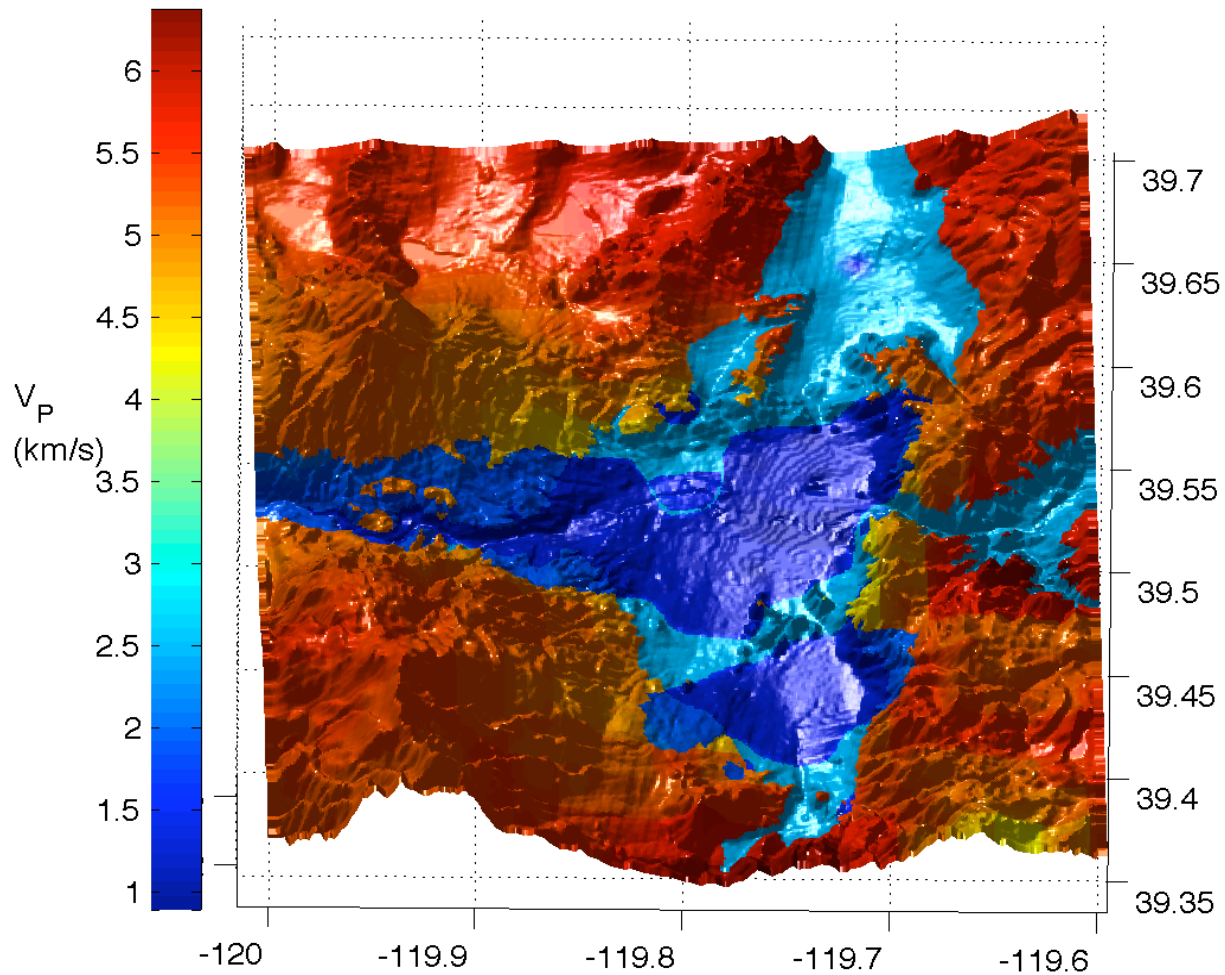


*Figure 4: P-wave velocity at an elevation of 1400 m on perspective view shaded relief. View is looking northward. Reno is situated primarily within the dark blue basin area.*

Observed waveforms were collected from the UNR Seismological Laboratory Antelope database and converted to SAC format. All traces are low-pass filtered with a corner frequency of 0.5 Hz. Not all events, especially the smaller ones, as would be expected, had enough signal within this passband to allow comparisons at all stations. All event magnitudes were converted to moment for input into E3D. If the estimated fault plane dimensions exceeded the grid node spacing (true for all events except event 4), a finite fault source was utilized in E3D; event 4 used a point moment source. A very simple self-similar scaling relationship was used to compute fault length and area from the magnitude that assumes fault length goes as the cube root of the moment ratios (Lay and Wallace, 1995). Double-couple focal mechanism solutions were available for all 6 events and were used in the computations.

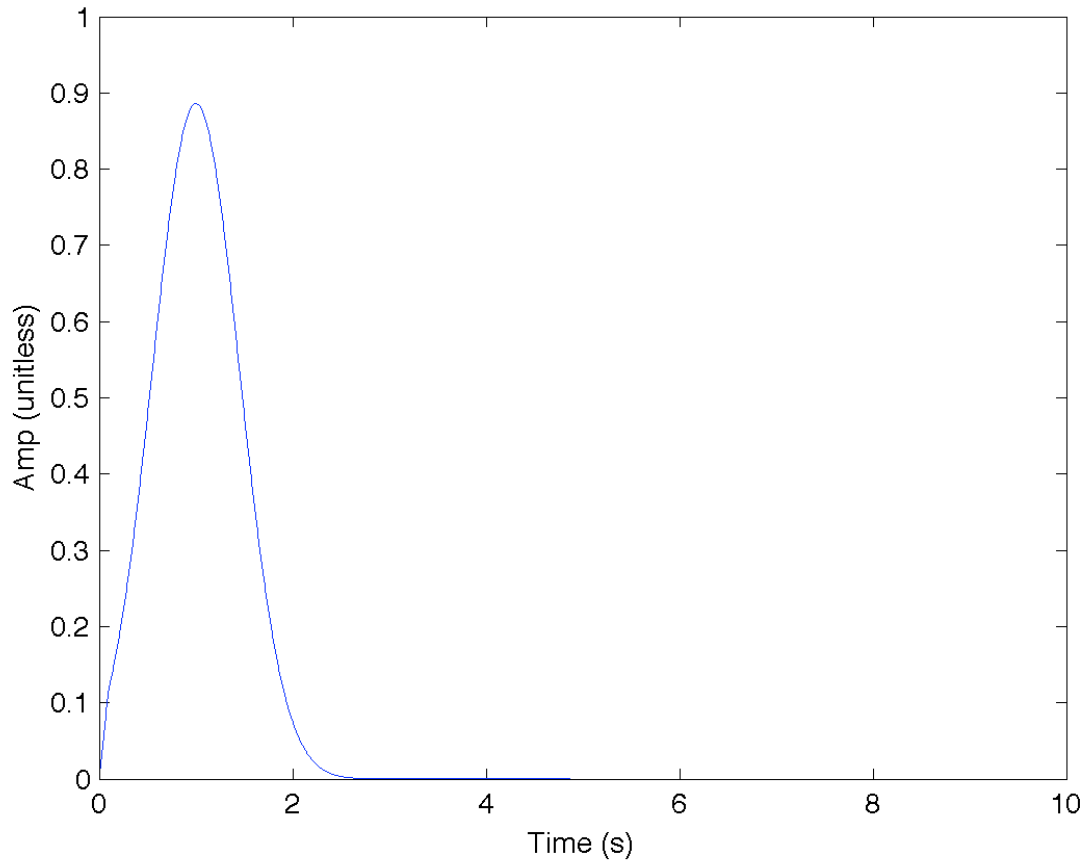


*Figure 5: Gaussian source-time function used in all the simulations.*

## Discussion

Synthetic waveforms from the old CVM with and without topography and the new CVM with and without topography were compared with observed waveforms. Comparisons were made at “raw” amplitudes and at various scalings in order to examine both amplitude and waveform shapes. Due to uncertainties in magnitude, all waveforms for a given event can be scaled to best match observations. Of importance here, though, is relative amplitude differences among different stations recording the same event. Waveform shape includes the duration of the wavetrain as well as relative amplitudes of different phases within the same trace.

Unfortunately, there is no clearly better model that works for all events and for all stations. There are instances where any of the four synthetic models match the observations better than any of the others. However, none of the models provide excellent fit to the observed waveforms. Only qualitative measures of fit can be used due to these deficiencies. Near offset receivers tend to show the best fit to observations, but in these cases, all four models can fit the data almost equally well. With these caveats, however, the new CVM with topography tends to produce the best fit to the observations, but it is only marginally better than the others.

The new models (both with and without topography) tend to predict the relative amplitudes of some of the P and early surface waves better than the old models, especially on the horizontal components, but again this is a tendency, not a rule and in certain cases the old models

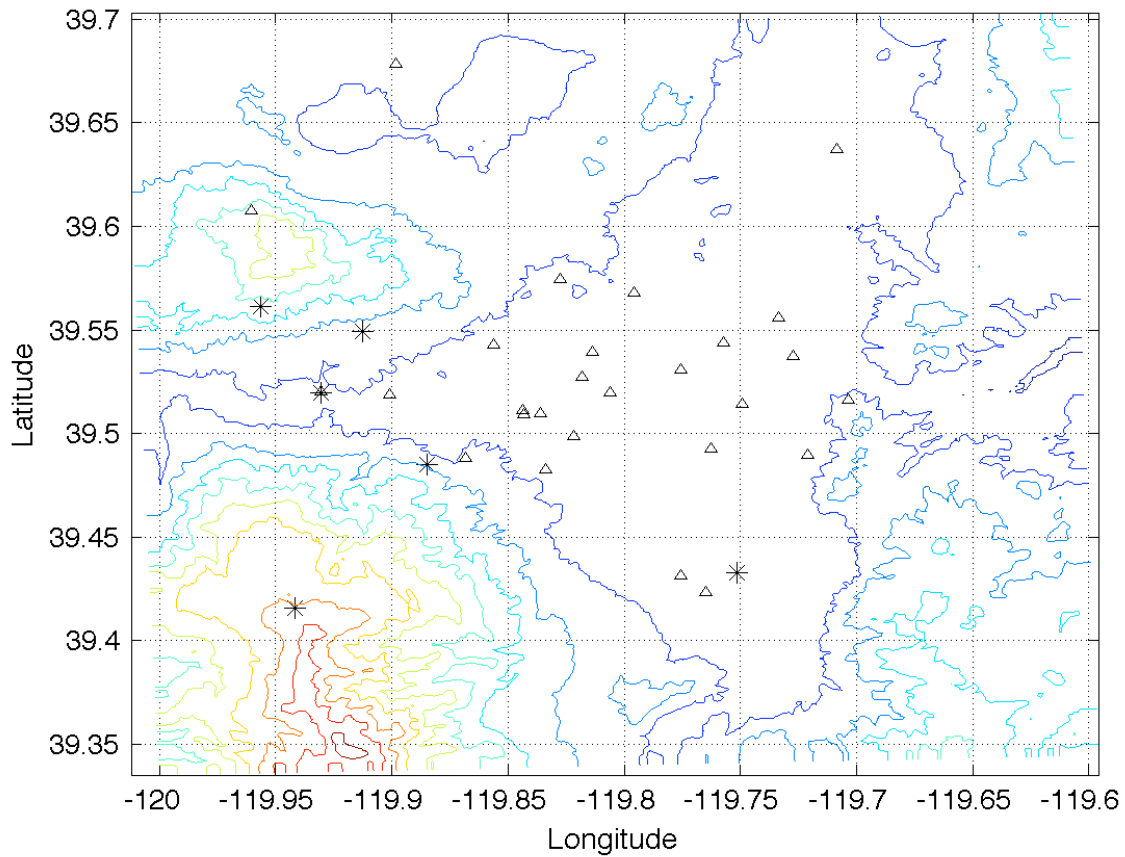


*Figure 6: Plan view of events (asterisks) and stations (triangles) used in the simulations shown over contoured topography. High terrain is indicated by red contours whereas low terrain is by blue contours.*

may provide better predictions. Even on the same station and event, one component may be better predicted by one model and another component by a different model. The models with topography (both old and new CVMs) tend to better predict the amplitudes of some of the later phases, but still underpredict wavefield duration. As a general rule, for a given event, the old CVM produces smaller amplitudes than the new CVM and models with topography produce smaller amplitudes, but longer duration, wavetrains than the models without topography. Some stations are over predicted in peak ground velocities, whereas others are under predicted, but there is no clear consistency among the events for any of the models.

One glaring deficiency in all of the models is the inability to predict the duration of the significant amplitude scattered wavefield. This worsens with increasing source-receiver offset. Several problems could contribute to this error: insufficiently sharp basin boundaries could allow too much energy to be leaked outside the basins instead of reflecting internally; excessive attenuation at these frequencies throughout the model; unmodeled small-scale structure that is creating more scatter than is modeled. Unfortunately, only station PEA, located on Peavine Peak, is situated outside a basin so it is difficult to assess basin versus non-basin effects. Even that station, however, probably due to its proximity to the basins, indicates prolonged scattering relative to the synthetics. It also is one of the worst fit receivers, except for event 6.

Filtering with the passband up to 0.1 Hz, improves the fit dramatically for some stations and events. However, this also removes much data since far fewer stations and events have significant energy within this passband for the observations. Another problem with this passband is that the differences among the models is greatly reduced making comparisons difficult. It still appears that even within this passband that the new CVM models do tend to produce better fits to the observations than the old CVM, especially the old CVM with topography which may exhibit some slight instabilities (oscillatory behavior) within this passband. Within the group of observations that are better fit with the new CVM models, some appear better fit with topography and others are better fit without topography. Unfortunately, errors in focal mechanisms can cause gross differences in the waveforms that only becomes clearly apparent within this lower frequency passband. It is noteworthy, though, that within this passband, there are some excellent fits of waveforms even though peak velocities still do not follow a clear pattern.

A higher resolution CVM is most likely necessary to produce more realistic waveforms. Although some information within the current CVM is at higher resolution, the tomography model (von Seggern and Preston, 2007) used to construct the new CVM has a maximum resolution of about 6 km. In general, the new CVM with topography does produce better results than the old CVM, but only marginally so and it still has glaring deficiencies. This result points to further fundamental deficiencies in our knowledge of the structure of the Reno-area basin, which we hope to resolve in future work.

## References

- Anderson, John G., Ileana Tibuleac, Abdolrasool Anooshehpour, Glenn Biasi, Kenneth Smith, and David von Seggern, 2009, Exceptional ground motions recorded during the 26 April 2008 Mw 5.0 earthquake in Mogul, Nevada: *Bull. Seismo. Soc. Am.*, 99, 3475-3486.
- Abbott, R. E., and J. N. Louie, 2000, Depth to bedrock using gravimetry in the Reno and Carson City, Nevada area basins, *Geophysics*, 65, 340-350.
- Clayton, R. and B. Engquist, Absorbing boundary conditions for acoustic and elastic wave equations: *Bull. Seismo. Soc. Am.*, 67(6), 1529-1540, 1977.
- dePolo, C. M., J. G. Anderson, D. M. dePolo, J. G. Price, 1997, Earthquake occurrence in the Reno–Carson City urban corridor: *Seismol. Res. Lett.*, 68, 401-412.
- Graves, R., Simulating seismic wave propagation in 3-D elastic media using staggered-grid finite differences, *Bull. Seismo. Soc. Am.*, 86, 1091-1106, 1996.
- Lay, T. and T.C. Wallace, 1995, *Modern Global Seismology*, Academic Press, San Diego.
- Louie, J., M. Heimgartner, A. Pancha, W. Thelen, J. Scott, and C. Lopez, 2006, A matter of scale: understanding Nevada's sedimentary basins for seismic hazard assessment: presented at Seismol. Soc. Amer. Ann. Mtg. and the Managing Risk in Earthquake Country Conference Commemorating the 100th Anniversary of the 1906 Earthquake, April 18 - 22, San Francisco, Calif.
- Olsen, K. B., Day, S. M., and Bradley, C. R., 2003, Estimation of Q for long-period (>2 sec) waves in the Los Angeles Basin, *Bulletin of the Seismological Society of America*, 93, 627-638.
- Pancha, Aasha, John G. Anderson, and John N. Louie, 2007, Characterization of near-surface geology at strong-motion stations in the vicinity of Reno, Nevada: *Bull. Seismol. Soc. Amer.*, 97, 2096-2117.



- Preston, Leiph, and David von Seggern, 2007, Joint seismic tomography/location inversion in the Reno/Carson City area: Final report to the National Earthquake Hazards Reduction Program, U. S. Geological Survey, Award Number 07HQGR0022, 18 pp., <http://earthquake.usgs.gov/research/external/reports/07HQGR0022.pdf>
- Schultz, C.A., A density-tapering approach for modeling the seismic response of free-surface topography, *Geophys. Res. Lett.*, 24, 2809-2812, 1997.
- Scott, J. B., M. Clark, T. Rennie, A. Pancha, H. Park and J. N. Louie, 2004, A shallow shear-wave velocity transect across the Reno, Nevada area basin, *Bull. Seismo. Soc. Amer.*, 94, no. 6 (Dec.), 2222-2228.
- Widmer, M. C., P. Cashman, J. Trexler and C. Benedict, 2007, Neogene through Quaternary stratigraphy and structure in a portion of the Truckee Meadows basin: a record of recent tectonic history, *Geol. Soc. America Abs. with Programs*, 39(4), 9.

## **Appendix**

### **Computing Green's Functions from Ambient Noise Recorded by Narrow-Band Seismometers, Accelerometers, and Analog Seismometers**

## **Computing Green's Functions from Ambient Noise Recorded by Narrow-Band Seismometers, Accelerometers, and Analog Seismometers**

D. H. von Seggern, I. M. Tibuleac, John G. Anderson and J.N. Louie,  
Nevada Seismological Laboratory, U. Nevada, Reno NV 89557  
[vonsegg@seismo.unr.edu](mailto:vonsegg@seismo.unr.edu); [ileana@seismo.unr.edu](mailto:ileana@seismo.unr.edu); [jga@seismo.unr.edu](mailto:jga@seismo.unr.edu); [louie@seismo.unr.edu](mailto:louie@seismo.unr.edu);

### **ABSTRACT**

Recovery of Green's Functions from ambient noise has typically used broad-band seismometer recordings such as obtained by the EarthScope Transportable Array. Our network at the Nevada Seismological Laboratory, like many networks, has an archive of recordings from instruments previously considered less suitable for recovery of Green's Functions. These sub-optimum instruments generally fall in one of three classes: 1) digital narrow-band seismometer recordings (for instance, S-13 seismometer), 2) analog narrow-band seismometer recordings, digitized after transmission, and 3) digital accelerometer recordings. Each of these classes presents its own problems for recovery of Green's Functions and requires appropriate processing.

Narrow-band analog recordings typically have a very narrow usable pass-band, with little accurate measurement of true ground motion at low frequencies ( $f < 0.2$  Hz) and have records often plagued by spikes and dropouts. On narrow-band digital recordings the combination of the inherent seismometer roll-off at  $< 1$  Hz and of too few counts per volt of seismometer output may lead to inadequate measurement of true ground motion at less than 1 Hz. We show that Green's Functions can be recovered on narrow band records at least in the microseismic frequency band and we discuss the digital signal processing methodology developed for this purpose. Accelerometers have a very different response from typical velocity-response seismometers. For instance, accelerometer recordings have a very large diurnal drift due to ambient temperature changes. Also, the instrument response discriminates against accurate recording of low-frequency ground motion. Yet, again, we show that Green's Functions can be recovered from station pairs including accelerometer sensors.

To process GF's extracted for inter-station pairs at less than 15 km and to resolve structure beneath arrays of close stations we make use of energy beams obtained by delay-and-sum methods. These techniques are applied on GF's extracted between a station and ad-hoc arrays within the Reno Basin. The inter-station distance is 15-100 km. First-order shear velocity models are estimated in the Reno Basin and the Reno-Carson area through inversion of phase velocity results.

## INTRODUCTION

To supplement the regional P/S 3-D velocity model in the Reno-Carson area we recover Green's Function estimates in the period band of 1-20 seconds from ambient noise cross-correlation of recordings from sub-optimum sensors such as the deployment in the Reno Basin (RB): narrow-band digital seismometers, analog-transmission seismometers, and accelerometers. We derive shallow crustal shear velocity models to fit the inter-station Green's Functions (GFs). GFs, with Rayleigh waves as the most prominent arrivals, are retrieved from ambient noise, which is usually ignored in traditional seismic data processing. We base our method on the fundamental observation that if A and B are two passive sensors (seismic stations), the GF, or the signal which B would receive when A is given an impulsive excitation, can be recovered from the temporal cross-correlation of incoherent noise received in A and B. Since this excitation is usually deeply buried in the ambient noise at random times and with random amplitudes, summation of the cross-correlations over a long time (months to years) is necessary to retrieve the Green's functions.

We demonstrate that, by using a variety of seismic sensors, high resolution estimates of ambient noise-derived shear - wave velocity models are possible for inter-station paths in high seismic hazard areas with a surface area of  $\sim 60 \text{ km}^2$ , such as the Reno Basin (Figure 1). In such small areas, a gap exists for demonstrated extraction of GF's from ambient noise between short and long inter-station distances. In other words, noise-extracted Rayleigh waves are currently sampling less than 0.2 km from the surface (Scott et al., 2004), or more than 8 km deep (Shapiro and Campillo, 2004; Lin et al., 2008). In order to estimate P and S velocity models deeper than 3 km, earthquake tomography (Preston and von Seggern, 2008) was until recently the only cost effective alternative to active source experiments (Frery et al., 2009). The tomographic studies in the Reno Basin (Preston and von Seggern, 2008) do not allow precise control of the low-velocity surface material depth in the basin, due to low resolution in the upper 3 km. Another disadvantage of S-wave tomography is the high level of uncertainty in the S-arrival time picks.

GFs are currently retrieved in the western USA from data recorded at broadband sensors, such as the EarthScope Transportable Array deployment (Figure 1, lower right plot) with resolution of 60-100 km (Yang et al., 2009; Shapiro et al., 2005; Sabra et al., 2005) for periods exceeding 8 s. Thus, the lateral resolution of existing tomographic models exceeds the dimensions of the Reno Basin area and the depth resolution is larger than the Reno Basin depth. GF extraction from noise crosscorrelations at scales less than 60 km sq. and using non-broadband instruments is possible and has been recently demonstrated by several research groups (Picozzi et al., 2009; Guedard et al., 2008).

To obtain higher resolution three-dimensional models, at less than 60 km scale, using ambient noise-extracted GF's, the density of broadband (we name BH, from the three-component channel names) stations must be increased considerably, which is not cost-effective, or, all the instruments available in the region must be used. The advantage of populated regions such as the Reno Basin is that dense networks of short-period instruments (analog or digital) and of accelerometers are already deployed (Figure 1, left

plot). This adds tens of stations, thus hundreds of inter-station paths to the broadband sensor information, with the potential to greatly improve velocity model resolution.

We define as "unconventional" a sensor pair containing at least one non-broadband sensor. As shown below, extracting useful data from unconventional sensor pairs is not a trivial exercise, and few research groups have attempted this type of study (Cho et al., 2007).

The first challenge in using unconventional sensor pairs is data quality. Short-period recordings often have poor data quality for the desired frequencies, especially "analog" recordings and the instruments are predominantly narrow-band (corner frequency  $\geq 1$  Hz) with the response rapidly decreasing at periods longer than 1 s. The accelerometer response de-emphasizes low frequencies ( $< 1$  Hz) and also accelerometers usually operate in trigger mode. In this study we show recovery of GF's from ambient noise for sensor pairs including: 1) digital narrow-band seismometer (EH) recordings (for instance, S-13 seismometer), 2) analog narrow-band seismometer (SH) recordings, digitized after transmission, 3) digital accelerometer (HG) recordings and 4) digital broadband instrument (BH) recordings, including USArray stations. Each of these instrument classes presents its own problems for GF recovery and requires appropriate processing.

Second, a significant challenge in using high density unconventional sensor pairs is that measurements of Rayleigh-wave phase and group velocity are difficult for stations separated by less than 15 km. The "rule of thumb" is that the longest GF Rayleigh wavelength that can be well-resolved is one-half to a one-third of the inter-station distance. For example, at 15 km distance, in order to extract Rayleigh waves from ambient-noise cross-correlations, noise spectra should contain sufficient energy at periods shorter than  $\sim 2$  sec.

If all the ambient noise were of oceanic origin, retrieving Rayleigh waves at shorter periods would be very difficult because the energy at these periods is low at distances greater than 100 km from the coast. Fortunately, although oceanic noise is the main ambient noise source, not all the ambient noise has oceanic origin (Frank et al., 2009). The advantage of populated regions is the presence of shorter-period cultural noise. Also, the advantage of rapid topographic changes, such as with the Sierra Nevada in the Reno vicinity, is an increase in short-period noise due to wind and due to topography scattering. Dense networks, like the Reno -Carson deployments, are usually installed in areas of high natural seismicity, thus with higher levels of background earthquake seismic noise. When used in ambient noise studies, the Reno Basin deployments have several other advantages: 1) they include densely spaced stations, thus the sampling depth for the Rayleigh waves is shallower (1 - 7 km) and 2) data is readily available (continuous recordings are available for accelerometers in Reno) and 3) data problems, if any, are well-known.

We have developed crosscorrelation algorithms (based on the work by Bensen et al., 2007) and new adaptations of array and network signal processing techniques to GF analysis. These algorithms can be applied to supplement the existing (BH sensor - derived) ambient noise GF data and the earthquake-derived information with tens-to-



hundreds of new inter-station paths. To extract GF's, our new data processing approach includes transformation of all waveforms into broadband velocity records, choosing waveforms likely to include seismic signals by application of analyst-chosen trace standard deviation thresholds and by continuous waveform pre-filtering as a function of inter-station distance. To process GF's extracted for inter-station pairs at less than 15 km and to resolve structure beneath arrays of close stations we make use of energy beams obtained by delay-and-sum methods (FK). These techniques are applied on GF's extracted between a station (at 15 - 100 km distance) and ad-hoc arrays within the Reno Basin, such as the ANSS accelerometers in Reno (Figure 1, left plot) or the Mogul RAMP broadband array (Figure 1, right plot). Phase velocity dispersion curves are inverted for first-order shear velocity models using the Computer Programs in Seismology (*surf96*) (Herrmann and Ammon, 2002).

## DATA

We process continuous waveforms recorded from 2007 to 2009 at Nevada Seismological Laboratory (NSL) and at EarthScope TA stations in Nevada. The permanent instrumentation deployed in the Reno Basin and vicinity consists of a 21 station, continuously recording, 10 km aperture accelerometer (HG) Advanced National Seismic System (ANSS) array, of several NSL digital short period (EH) sensors, of several analog – transmission short period sensors (we name “analog” or SH) and of three broadband (BH) sensors (Figure 1, left plot). This setting, ~ 60 km in scale, is different than the uniform instrumentation, broadband networks of hundreds of km aperture where GFs are usually retrieved (Figure 1, lower right plot). The network includes (Figure 1, upper right plot) a temporary Rapid Array Mobilization Program (RAMP) array of portable broadband stations, named the Mogul Array installed in Mogul, West Reno to record an earthquake swarm in 2008 (Anderson et al., 2009). To illustrate data quality, we also use continuous waveforms recorded at stations within the Southern Great Basin Digital Seismic Network (SGBDSN) in 2007 and 2008 because they have the advantage of co-located HG, SH and EH sensor deployments.

## METHOD

### Green's Function retrieval from "unconventional" sensor pairs

The unconventional deployments have significant disadvantages:

1. *Narrow-band analog recordings* (SH) typically have a very narrow usable pass-band, with supposedly less accurate measurement of true ground motion at low frequencies ( $f < 0.2$  Hz) and have records often plagued by spikes and dropouts. The combination of seismometer response roll-off at  $f < 1$  Hz and of too few counts per volt of seismometer output should lead to inadequate measurement of true ground motion. The records are affected by datalogger noise and transmission noise.
2. *Short-period digital recordings* (EH) are predominantly narrow-band (corner frequency  $\geq 1$  Hz) with response rapidly decreasing at frequencies lower than 1 Hz.
3. Investigations using *accelerometer recordings* (HG) have to overcome several obstacles: 1) a very large diurnal drift due to ambient temperature changes; 2) the instrument response (with 1 Hz corner frequency) discriminates against faithful recording

of low-frequency ground motion; 3) removing the instrument response to obtain displacement is not a trivial exercise. The displacement derived from accelerometers is often unstable at long periods, as a double integration is required. Accelerations at long periods are very small, thus the signal to noise is low; 4) unlike the RB ANSS deployment, accelerometers in other locations usually operate in trigger mode; 5) the existence spurious noise, or "bad noise".

#### Experiments for methodology development

*"Good" versus "bad" noise.* "Good" noise is usually Earth seismic noise, cultural noise and atmospherically induced noise. In order to obtain the same results with different types of sensors, the recorded noise should be coherent, within the frequency range of interest, at the same location. Our investigations show that accelerometer-recorded noise at periods longer than 1 sec is not correlated with the noise recorded by short-period instruments in the same frequency band.

A comparison of waveforms recorded at three different types of sensors is shown in the left plots of Figure 2. These co-located sensors are currently operating at the SGBDSN station Wildcat (WCT/WLD) in southern Nevada, near Yucca Mountain. The response is reshaped to a broad-band sensor response with a corner at 10-s period, high passed at 0.05 Hz. In the upper left plot, the first waveform is recorded on a SHZ channel of a Mark Products L-4 short-period sensor digitized at NSL. The middle left waveform is recorded at digital EHZ-type channel of a Geotech S-13 sensor with 1-Hz natural frequency. The bottom left waveform is a digital accelerometer HGZ channel recording. These waveforms are zero-phase, four-pole Butterworth filtered from 0.1 - 1 Hz and are represented in the same order in the lower left plot. Only the EHZ and SHZ traces show coherent long-period energy. The right upper plot of Figure 2 shows the HG sensor noise spectrum which is different from the observed noise spectrum of the EH and SH (for the waveforms in the left plots). A good measure of whether recordings from differing instruments are reproducing ground motion is coherence. We use the Matlab<sup>®</sup> function "mscohere" for the magnitude squared coherence estimate of two signals, using Welch's averaged, modified periodogram method (Stoica and Moses, 1997). The magnitude squared coherence (we name coherence) estimate is a function of frequency with values between 0 and 1 that indicates how well the two signals correspond to each other at each frequency. Figure 2, bottom right plot, shows the coherence between the raw traces in the left plots. The EHZ and SHZ components are recording ground motion above noise levels for frequencies below 1 Hz. At these frequencies, the lack of coherence of the EHZ-HGZ and SHZ-HGZ components shows that the HGZ component at this site is recording mainly instrument noise. Note improved coherence at 1 Hz for all pairs of sensors.

Our interpretation of the above experiments is that, unlike BH recordings, at frequencies below 1 Hz, the HG recordings are affected by internally generated self-noise (sensor noise). **The presence of HG instrument noise is indicated by low coherence among the three sensor components, constant noise spectrum variance observed after the instrument is removed, and by the shape of the HG spectrum, resembling the shape of a white spectrum convolved with the response of a broadband seismometer (Figure 2, right upper plot).** Internal noise can make the recovery of GF's from continuous HG data difficult. When earthquake seismic signal is present, it is well-known, however, that longer-periods

(> 5 sec) are recorded by accelerometers. This observation is important because most accelerometers are operating in trigger mode. As shown by Yao et al., (2009), using only event records on broadband stations can lead to extraction of GF's similar to those extracted from continuous noise. Thus, because only records with Earth signals are useful, accelerometers could be successfully used for GF's retrieval, even in trigger mode, proved that enough triggered data is available. Accelerometer pairs at distances greater than 20 km were successfully used, with certain signal processing precautions, by Cho et al. (2007) to extract ambient noise GF's in the Korean Peninsula.

An experiment using different processing time lengths for a pair of SH sensors has shown improvement in the GF signal-to-noise ratio (SNR) with increasing of the analysis time length. Unlike at the broadband sensors, stacking at analog sensors needs to be for longer than 1 year in order to obtain good GF SNR. Figure 3 shows GF retrieval for different stacking time lengths (one month, three months, one year and two years) for a pair of analog sensors SMI (SHZ), and TAH (SHZ). Station locations are shown in Table 1. The possibility of GF P-component retrieval (Figure 3, lower plots and Figure 4) is discussed below.

The approach we take in processing unconventional sensor records includes:

- 1) High pass signal filtering at 0.05 Hz with a zero-phase, 4 pole Butterworth filter to remove accelerometer record drift;
  - 2) Apply an analyst-chosen threshold on acceptable waveform variance to restrict the accelerometer records used to waveforms including ground motion signal as opposed to only accelerometer internal noise;
  - 3) For all sensors, reshape the response to a broad-band velocity sensor response with a corner at 10-s period. We have chosen the 10 s period since 10 sec fundamental mode Rayleigh waves are the longest waveforms we expect at inter-station distance < 100 km. This procedure also eliminates the usual challenges related to signal distortion resulting from accelerometer instrument removal (Iwan et al., 1985).
  - 4) Choose specific pre-filtering frequency bands as a function of inter-station distance;
  - 5) Use longer periods (one year or two) of continuous data at short period instruments;
- Our processing includes use of the Bensen et al., 2007 sign-bit convention, without pre-whitening (all positive amplitudes = +1 and all negative amplitudes = -1).

#### Green's Function Processing

The "rule of thumb" is that the inter-station distance should be at least three times to several tens of times larger than the maximum wavelength of the Rayleigh seismic phases of interest. Thus, the depth probed is usually 1/3 of the Rayleigh phase wavelength.

For inter-station distance < 15 km, we form ad-hoc arrays of stations within the Reno Basin and we estimate the fundamental mode Rayleigh phase velocity from the energy beam for all points in 2D wavenumber space (FK). For inter-station distance > 15 km, the retrieved GF's are inverted with a set of traditional inversion programs for shear velocity structure in the Reno Basin. Rayleigh-wave dispersion curves are estimated and inverted using the vertical component GF's, with the Computer Programs in Seismology (CPS3.3), version 3.30 (2002) by R. Herrmann, C. Ammon, and their students.

## RESULTS

### Green's Function retrieval from "unconventional" sensor pairs

Short-period digital sensor EGF retrieval. Figure 5, upper right plot, shows the record section of recovered GF's for ten SGBDSN inter-station paths (Figure 5, left plot). The record section representation in  $FK$  space is shown in the bottom right plot. By tracking the fundamental and possibly, the first higher mode, several points in a dispersion curve (velocity versus period) can be extracted and used for inversion. The period band of useful information is from 5 s to 10 s. Since the scope of this example is only to demonstrate the EH-EH pair GF retrieval, seismic velocity model inversion for the Yucca Mountain region will be the subject of future investigations.

GF retrieval for pairs of narrow-band analog recordings (SH) and SH, BH, HG sensors. In Figure 6 we show that GF's can be recovered on narrow-band analog records at least in the microseismic frequency band. Station locations and path information are listed in Table 1. Although analog stations have only vertical components, there is a significant amount of new information that can be extracted from GFs' observed Rayleigh waves. P - arrivals and Rayleigh higher modes are identified in the  $FK$  plots in Figure 6 only, although the filter applied to the GF's in the left plots of Figure 6 does not allow visualization of these arrivals. A possible explanation for identification of these arrivals uniquely for this station configuration is related to the VPK station location at the boundary between the Sierra Nevada Range and western Great Basin. At this type of boundaries, fundamental mode Rayleigh waves in the noise are likely to scatter into higher modes.

### GF retrieval for pairs of broadband recordings (BH) and SH, BH, HG sensors.

In Figure 7 we show GF's retrieved for paths from broadband sensors such as P07A to stations in the Reno area (Figure 7a) and PAH (Figure 7b) to ANSS accelerometers in the Carson area, south of Reno. When compared to the Priestley and Brune (1978) model both transects show lower phase velocity. When compared to the average measurements at each period, slightly lower velocity Rayleigh phase velocity in the Reno-Carson area is observed by Lin et al. (2008) for periods larger than 8 s (i.e. sampling deeper than 8 km). We plot in Figure 8 the GF's for similar paths from the TA station P06A to BMHS (BH) and PICO (HG) (see also the line in Figure 1). BMHS and PICO are within 1 km of each other. We find very good correspondence of the GF's extracted for the two paths, on all three components.

GF retrieval for pairs of closely-spaced sensor (array aperture  $< 10$  km). To obtain information beneath ad-hoc arrays of stations within the Reno Basin we consider stations outside the Reno Basin as "sources", with the empirical requirement that the "array" aperture is less than five times the "source"- "array" distance. A delay-and-sum method is applied to form the energy beam for all points in 2D wavenumber space ( $FK$ ), for GF's "recorded" at the array stations from the "source" and fundamental-mode Rayleigh wave phase velocity across the ad-hoc arrays is estimated. As shown in Figures 6-10, the GF Rayleigh waves are almost monochromatic, with period depending on the path length

(the longer the inter-station distance, the longer the period, thus the deeper the sampling of the structure beneath the array). On the FK plots in Figures 6-10 the shortest period is empirically chosen such that the inter-station distance should be greater than at least two Rayleigh wavelengths. For each station considered as "source", the extracted GF record section (left plot) and phase velocity dispersion curve information for the corresponding ad-hoc array (right plot) are shown in Figure 9 for the ANSS stations and in Figure 10 for the Mogul stations. The quality of the FK plots and of the GF's is better for the ANSS HG array, even if the Mogul array is composed of BH stations. A possible explanation is the two month continuous record availability at Mogul sensors versus three year continuous record availability at the ANSS array. Another possible explanation, and the subject to future investigations, is the contribution of factors such as the small-array aperture, pre-filtering and data sampling to the quality of the results.

Retrieval of GF P-component. Although P - arrival retrieval is not the scope of our study, thus we take no data processing precautions aimed at P-arrival extraction, we interpret observations in Figures 3 and 5 as the P GF component. An intriguing observation in the lower four plots of Figure 3 is the retrieval of a short period P phase (0.5 - 2 Hz) arriving 2.8 sec before the time of a model-predicted Pg arrival (6 km/s). The group velocity of the phase we interpret as a P-arrival is 7.8 km/s and is consistent to a travel path through the Sierra Nevada roots. It seems interesting that the arrival we interpret as P in Figure 3 is retrieved on the crosscorrelation beam side without a Rayleigh wave - dominated GF. Thus, we retrieve several possible GF P components, as shown in Figure 4. The results show that the above observation cannot be expected in all cases.

#### First-order shear velocity models in the Reno Basin and in the Reno-Carson area.

Starting with models inspired by Priestley and Brune (1988) and shown in Table 2, and using the CPS3.3 algorithms, we invert the interpolated (Figure 11) phase velocity measurements to derive shear -velocity models beneath the 4 km aperture Mogul array (Figure 11a) and beneath the 10 km aperture ANSS array (Figure 11b) in the Reno Basin. A global model of the Reno-Carson area is derived using the interpolated value (Figure 11c) of the phase velocity derived from measurements in Figure 6a, Figure 7, Figures 9-10 and Table 1. Measurements are available for periods between 1 s and 8 s, with a gap at 4 s period. We estimate the median velocity value in 0.5 km/sec bins and we linearly interpolate the median values for the missing periods. The estimated first-order shear -velocity models are shown in Table 3. The shear velocity value derived for the upper one km thick layer the Reno Basin is 1.6 km/s. According to results of a study by Campbell, 2009 this value is consistent to shear velocity in sedimentary basins at more than 600 m depth and is lower than the hard-rock shear-wave velocity of 2 km/s.

## **CONCLUSIONS**

We recover GF's from cross-correlation of ambient noise data in western Nevada using continuous data recorded at unconventional instruments managed by the NSL, as opposed to using only the three broadband seismometers available in the area. We process analog narrow-band seismometers, digital narrow-band seismometers, and accelerometers from the NSL seismic archive. Each sensor type needs a specific processing approach. We



reshape the sensor responses to that of a broadband seismometer. Because of the prevalence of instrumental and cultural noise in recordings of these types of instruments, a longer time period of ambient noise must be processed to begin to recover what would normally be recovered from broadband seismometers in a month or two of recording.

We show that we can obtain useful FR dispersion data in the period range of 1-8 s from these unconventional instruments. Our results show that, except for 4 s period, enough noise energy is recorded at periods shorter than 8 sec to extract FR GF's. We have encouraging results in identification of first higher mode Rayleigh waves and in extraction of the P - component of the GF's.

The estimated FR dispersion results show fair agreement with dispersion curves previously published for the Great Basin, however, as expected, the phase velocity is lower at the respective periods. We estimate shear velocity values in the Reno-Basin and Reno-Carson with are consistent with the basin geological structure.

### **Acknowledgements**

This work was supported by NEHRP Grant # 1320 114 113X administered by the U.S. Geological Survey.

### **REFERENCES**

- Anderson, J. G., I. Tibuleac, R. Anooshehpour, G. Biasi and K. Smith (2009), exceptional Ground Motions Recorded During the 26 April, 2008, MW=5.0 Earthquake in Mogul, Nevada, *Bull. Seism. Soc. Am.*, **99**, No. 6, 3475–3486, doi: 10.1785/0120080352
- Campbell., K. W., 2009. Estimates of Shear-Wave Q and  $\kappa_0$  for Unconsolidated and Semiconsolidated Sediments in Eastern North America, *Bull. Seism. Soc. Am.*, **99**, No. 4, 2365–2392.
- Frery, R.N., Stephenson, W.J., Louie, J.N., Odum, J.K., Maharrey, J.Z., Messmer, M.L., Tomlinson, I., Littlefield, E.F., Hughes, A., Jha, S., Kohls, K., Dhar, M.S., Konkol, S., Wakwak, A., Cashman, P.H., Trexler, J.H., Kent, R., Hoffpauir, C., 2009. Preliminary analysis of high-resolution seismic imaging profiles acquired through Reno, Nevada, for earthquake hazard assessment, Abstract.
- Herrmann, R.B., Ammon, C.J., 2002. Computer Programs in Seismology – SurfaceWaves, Receiver Functions and Crustal Structure. Saint Louis University, <http://www.eas.slu.edu/People/RBHerrmann/ComputerPrograms.html>.
- Preston, L., and D. von Seggern, Joint Seismic Tomography/Location Inversion in the Reno/Carson City Area, Final Report to the National Earthquake Hazard Reduction Program, U. S. Geological Survey Award Number 07HQGR0022, 2008.
- Picozzi, M., S. Parolai, D. Bindi and A. Strollo, 2009. Characterization of shallow geology by high-frequency seismic noise tomography, *Geophys. J. Int.* (2009) **176**, 164–174 doi: 10.1111/j.1365-246X.2008.03966.x.

- Priestley, K and J. Brune, 1978. Surface waves and the structure of the Great Basin of Nevada and western Utah, *JGR*, v. 83, pp. 2265-2272.
- Scott, J. B., M. Clark, T. Rennie, A. Pancha, H. Park and J. N. Louie, 2004, A shallow shear-wave velocity transect across the Reno, Nevada area basin, *Bull. Seism. Soc. Am.* 94, no. 6, 2222-2228.
- Smith, K., von Seggern, D. H., dePolo, D., Anderson, J. G., Biasi, G. P., Anooshehpour, R., (2008), Seismicity of the 2008 Mogul-Somerset West Reno, Nevada Earthquake Sequence, *Eos Trans. AGU*, 89(53), Fall Meet. Suppl., Abstract S53C-02.
- Stoica, P., and R. Moses. Introduction to Spectral Analysis. Upper Saddle River, NJ: Prentice-Hall, 1997. Pgs. 61-64.
- Tibuleac, I.M., and E.T. Herrin (1999). An automatic method for determination of Lg arrival time using wavelet transforms, *Seism. Res. Lett.* 70, 577-595
- Tibuleac, I. and J. Britton (2006), An Automated Short-Period Surface-Wave Detection Algorithm, *Bull. Seis. Soc. Am.* **96**, 334-343
- von Seggern, D.H., Tibuleac, I.M., J. G. Anderson and Louie, J.N, 2009. Computing Green's Functions from Ambient Noise Recorded by Narrow-Band Seismometers, Accelerometers, and Analog Seismometers, abstract presented at the 2009 Annual Meeting Announcement Seismological Society of America, 8–10 April 2009 Monterey, California
- Yang, Y., M.H. Ritzwoller, F.-C. Lin, M.P. Moschetti, and N.M. Shapiro, 2009. The structure of the crust and uppermost mantle beneath the western US revealed by ambient noise and earthquake tomography, *J. Geophys. Res.*, in press.
- Yao, H., R. D. van der Hilst and M. V. de Hoop, 2006. Surface-wave array tomography in SE Tibet from ambient seismic noise and two-station analysis – I. Phase velocity maps, *Geophys. J. Int.* (2006), 166, 732–744
- Yao, H., Beghein, C., and Van der Hilst, R.D., 2008. Surface-wave array tomography in SE Tibet from ambient seismic noise and two-station analysis: II – Crustal and upper-mantle structure, *Geophys. J. Int.*, Vol. 163, 205-219, doi: 10.1111/j.1365-246X.2007.03696.x.

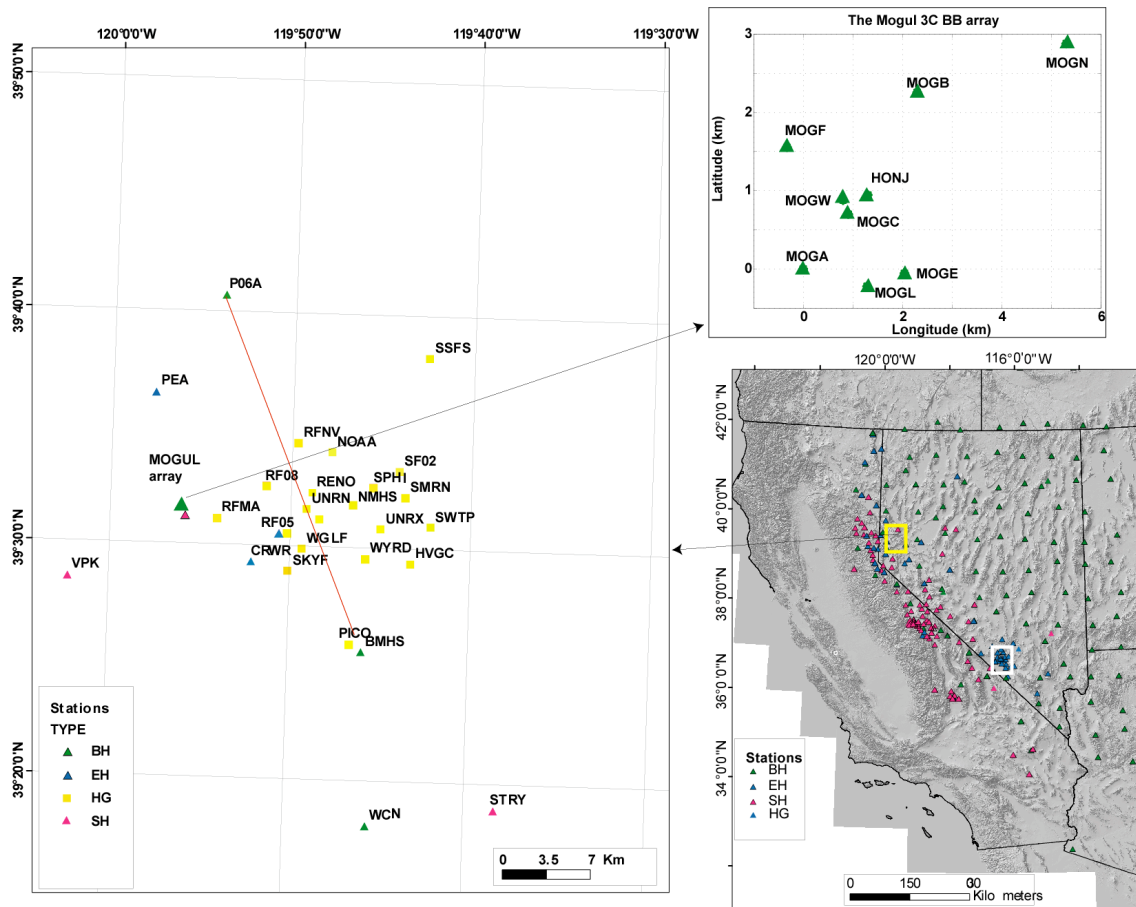


Figure 1. Left plot: The Reno Basin station location (BH - broadband sensors are shown as green triangles, EH - short period sensors are shown as blue triangles, SH - analog short period sensors are shown as magenta triangles and HG - accelerometers are shown by yellow squares). The upper right plot shows the Mogul RAMP deployment of broadband sensors in Mogul, Reno. The lower right plot shows the network of instruments with continuous records available at the Nevada Seismological Laboratory. The green triangles show locations of the 3C broadband components of the Transportable Array EarthScope deployment. The sensors are shown with the same color code as in the left plot. The yellow, respectively white rectangles in the lower right plot show the Reno area (in the left plot) and the Southern Great Basin Seismic Network area. A red line shows a path from BH station P06A to an accelerometer (PICO - HG) ~ 1 km apart from a BH sensor (BMHS).

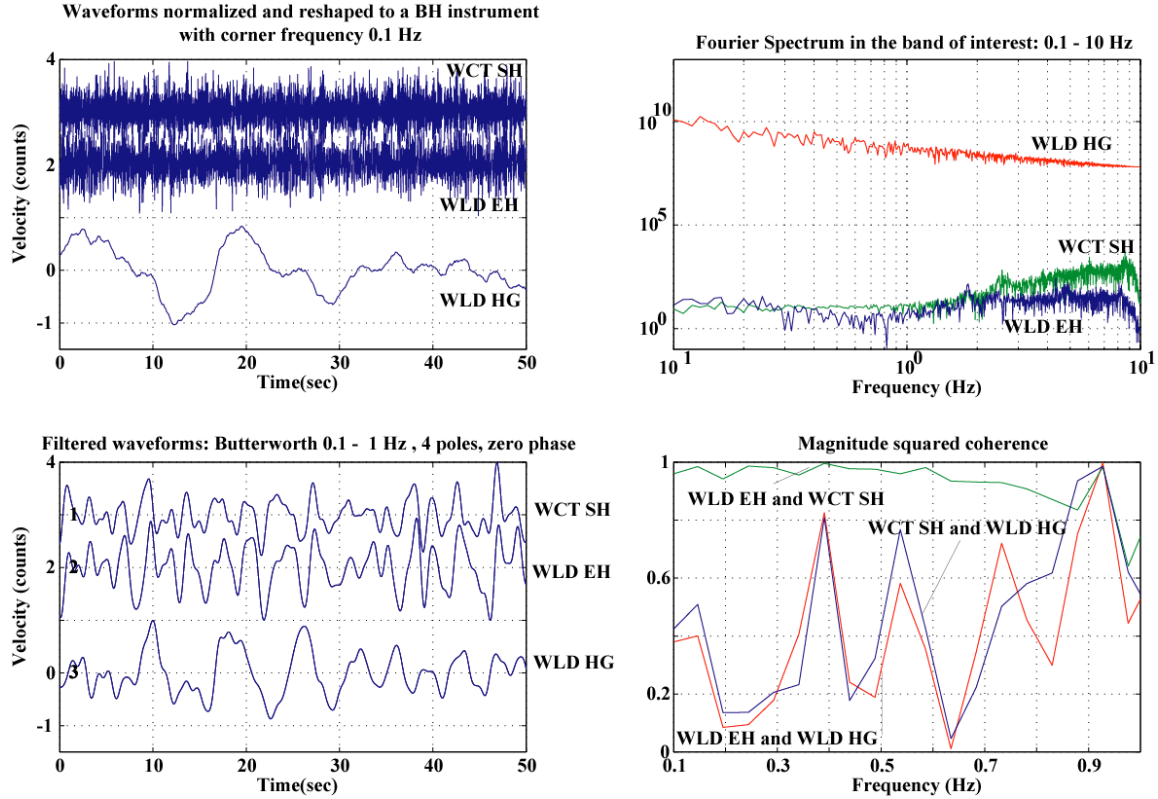


Figure 2. Recordings at co-located instruments at Wildcat Mountain (36.7928 N, 116.6257 W), near Yucca Mountain, Nevada. The left top plot shows the raw traces after being reshaped to a BH instrument with corner frequency 0.1 Hz. The bottom left plot shows the same traces as in the upper left plot filtered in the frequency band of interest for our study (0.1 - 1 Hz). The instruments are WLD:EHZ (EH), a narrow-band digital seismometer (L4), WCT:SHZ (SH), a narrow-band analog seismometer (S-13), and WLD:HGZ (HG), a digital accelerometer (131A\_02 MEMS). The upper right plot shows the Fourier spectrum in the band of interest for the HG (red), EH (blue) and SH (green) sensors, after being reshaped to a BH instrument with corner frequency 0.1 Hz. Note the lack of similarity of the HG spectra when compared to the EH and SH spectra. The bottom right plot shows the magnitude squared coherence (with a maxim value of 1) for pairs of sensors in the frequency band of interest. While the short-period sensor recordings(WCT SH and WLD EH) are coherent at frequencies lower than 1 Hz (green), the accelerometer noise and the noise recorded by the short-period instruments(blue and red) are not coherent at all frequencies below 1 Hz. The HGZ component at this site is apparently recording mostly instrument noise.

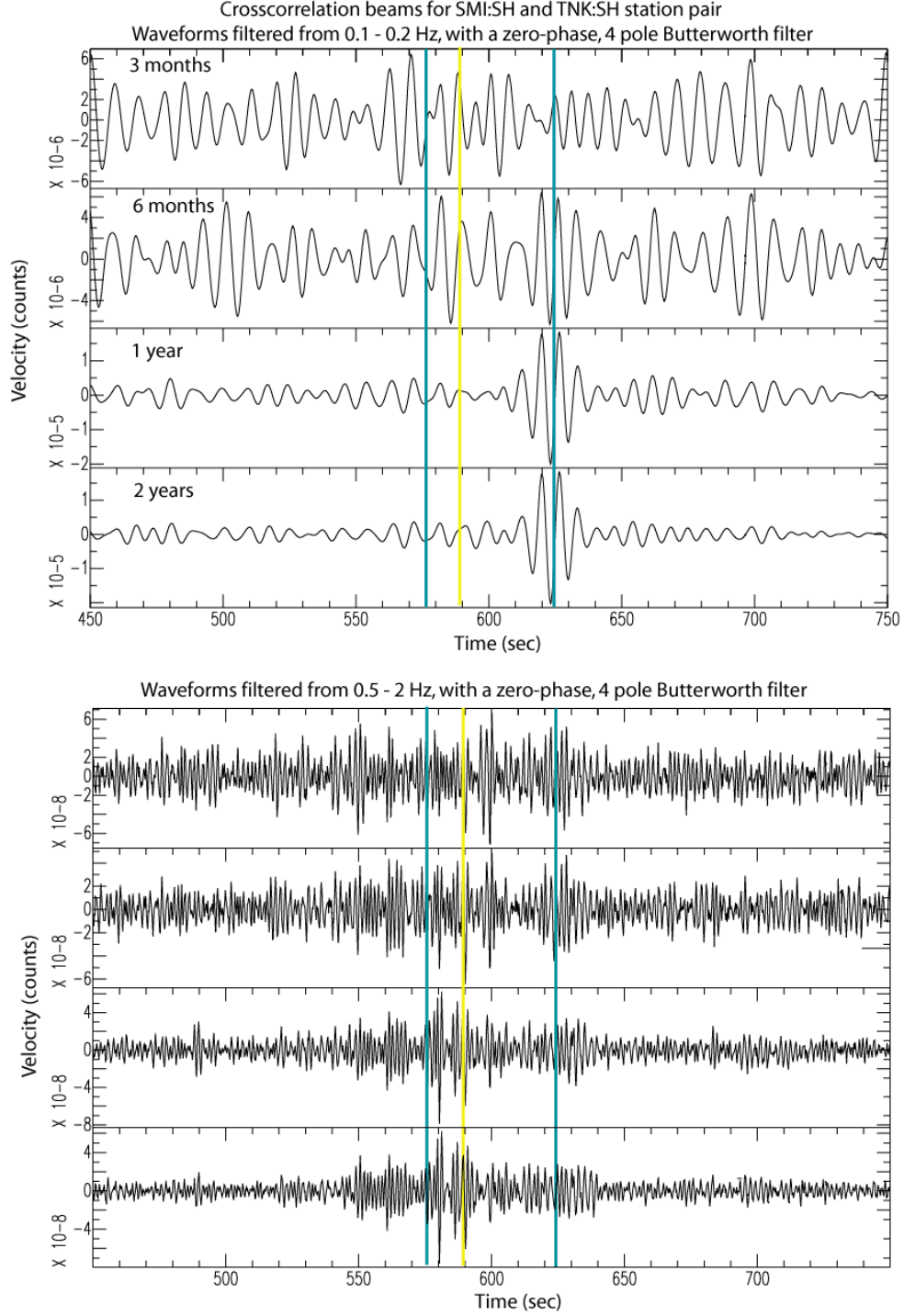


Figure 3. GF extraction for analog sensor pairs (Table 1) is possible, however, for a longer analysis time length ( $\sim 1$  year) than the one ( $\sim 3$  months) necessary for broadband pair GF extraction. The upper four plots show two-sided crosscorrelation stacks for an analysis period of 3 months, 6 months, one year and respectively two years. The blue line at 23.6 s time lag shows the expected arrival time of a 3 km/s Rayleigh phase. Note the crosscorrelation asymmetry in the upper plots. The yellow line shows the expected arrival time of a 6 km/s Pg phase (11.8 s) from a distance of 71.3 km. We interpret the higher frequency (0.5 - 2 Hz) arrivals emerging from noise at  $\sim 9$  s time lag in the lower

four plots as early, crustal first  $P$  arrivals, possibly due to higher velocity in the Sierra Nevada crust. Note the presence of these arrivals on the opposite side of the crosscorrelation trace from the Rayleigh wave-dominated GF.

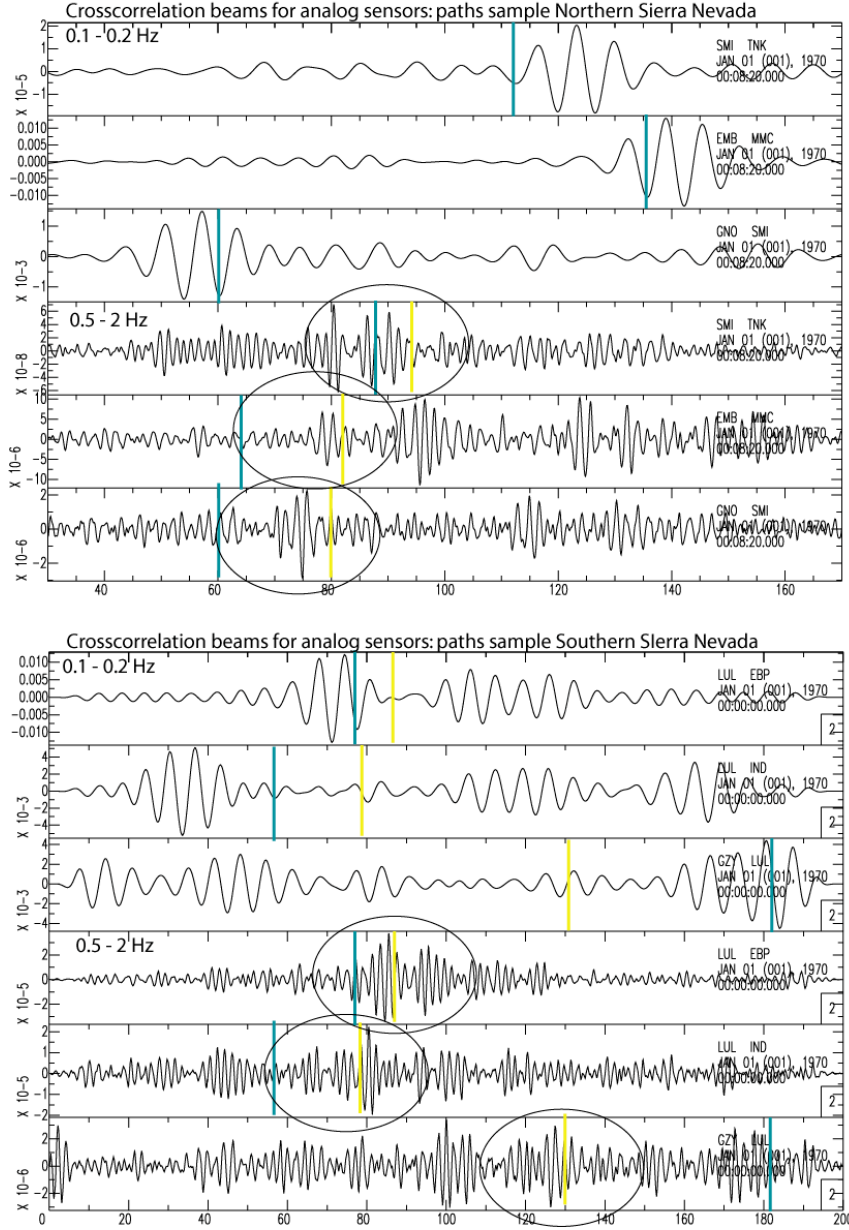


Figure 4. GF extraction for pairs of analog sensors for stations pairs in the northern (upper inset) and southern (lower inset) Sierra Nevada Range. The dominant, Rayleigh wave GF component (0.1 - 0.2 Hz) is shown in the upper three plots of each inset. The largest short-period arrivals in the lower three plots of each inset are interpreted as the  $P$  component of the Green's function. The  $P$ -component is identified on the same side of the crosscorrelation trace with the visible Rayleigh GF for all station pairs except SMI-TNK (see also Figure 3). Time lags for the blue lines are estimated using the inter-station distances in Table 1 and 3 km/s Rayleigh velocity. Time lags for the yellow lines are estimated using the inter-



station distances in Table 1 and 6 km/s Pg velocity (distances < 150 km), or 8 km/s Pn velocity for stations farther than 150 km (at stations GZY-LUL and LUL - IND).

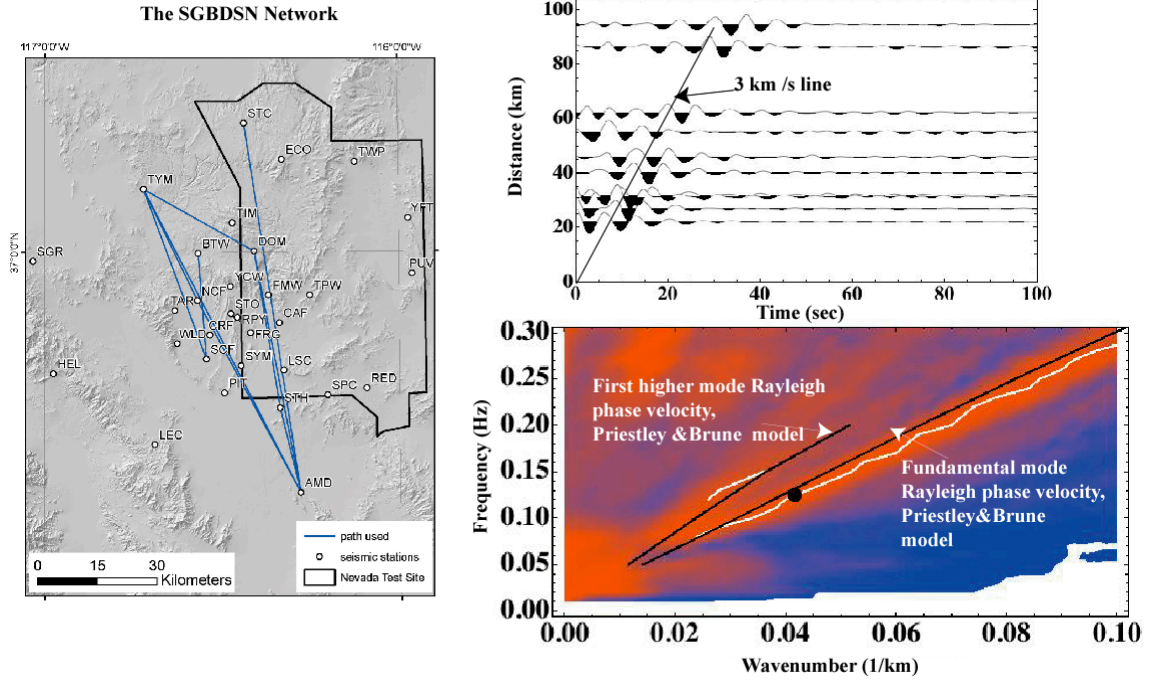


Figure 5. Retrieval of GF's from pairs of digital short-period instruments (EH) at the Southern Great Basin Digital Seismic Network (SGBDSN) near the Nevada Test Site. The left plot shows station location and the inter-station paths. The top right plot shows the retrieved GF's on the vertical components for one year of data, filtered with a four-pole, zero phase Butterworth filter. The black line marks the time lag for 3 km/s velocity. The lower right plot shows the FK plot for the record section above. The fundamental and 1st higher modes are tracked in white, as the maxim value of the beam energy at each wavenumber. The reference curves from the Priestley and Brune (1978) are black, and the dot is from ambient noise results of Lin et al, (2008). Note lower Rayleigh phase velocity at Yucca Mountain compared to the velocity predicted by the reference model.

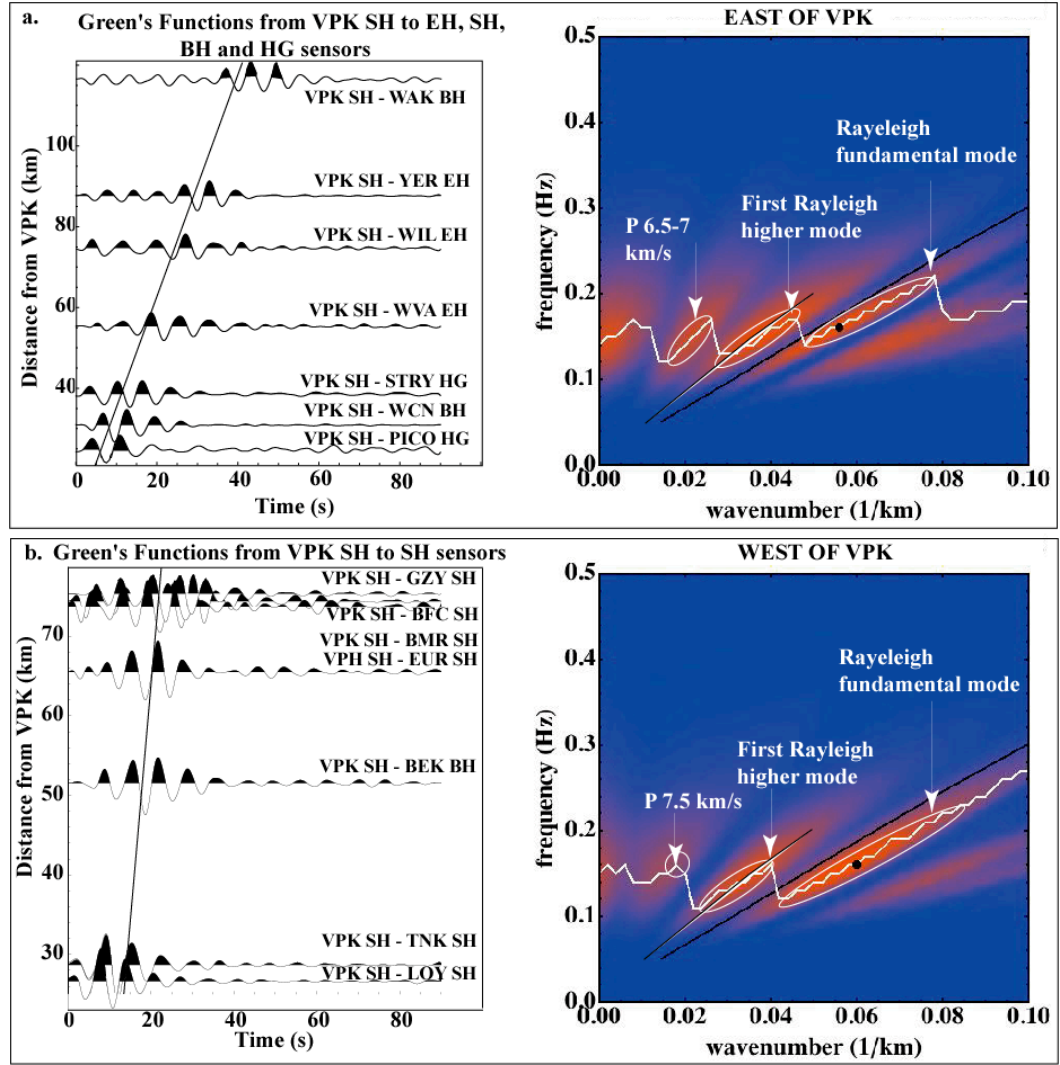


Figure 6. Record sections of recovered GF's filtered using a 0.1 - 1 Hz four pole, zero phase Butterworth filter, for station pairs including an analog seismometer at station VPK are shown in the left plots of each inset. The FK analysis for these record sections is shown in the right plots. The white trace on the FK plots shows the maxim FK value for each wavelength. The region sampled in the upper inset includes the Reno-Carson basins, east of VPK. The region sampled in the lower inset is in the Northern Sierra Nevada, west of VPK. Station locations are shown in Table 1 and phase velocity dispersion curves are shown in Table 2. The inter-station distance varies from 22 to 120 km. The black line in each of the left plots shows the 3 km/s time lag for the Rayleigh phases. The reference dispersion curves in the right plots (black lines) show the fundamental (FR) and first higher mode Rayleigh (HR) dispersion curves estimated using the Priestley and Brune (1988) model. We identify P, HR and FR waves in both insets. The values in the white ellipses are shown in Table 2 for each phase. Note lower values of the FR phase velocity in the Sierra Nevada shallow (< 7 km depth) crust than in Reno-Carson area shallow crust. The black dot marks the largest amplitude value in each FK plot.



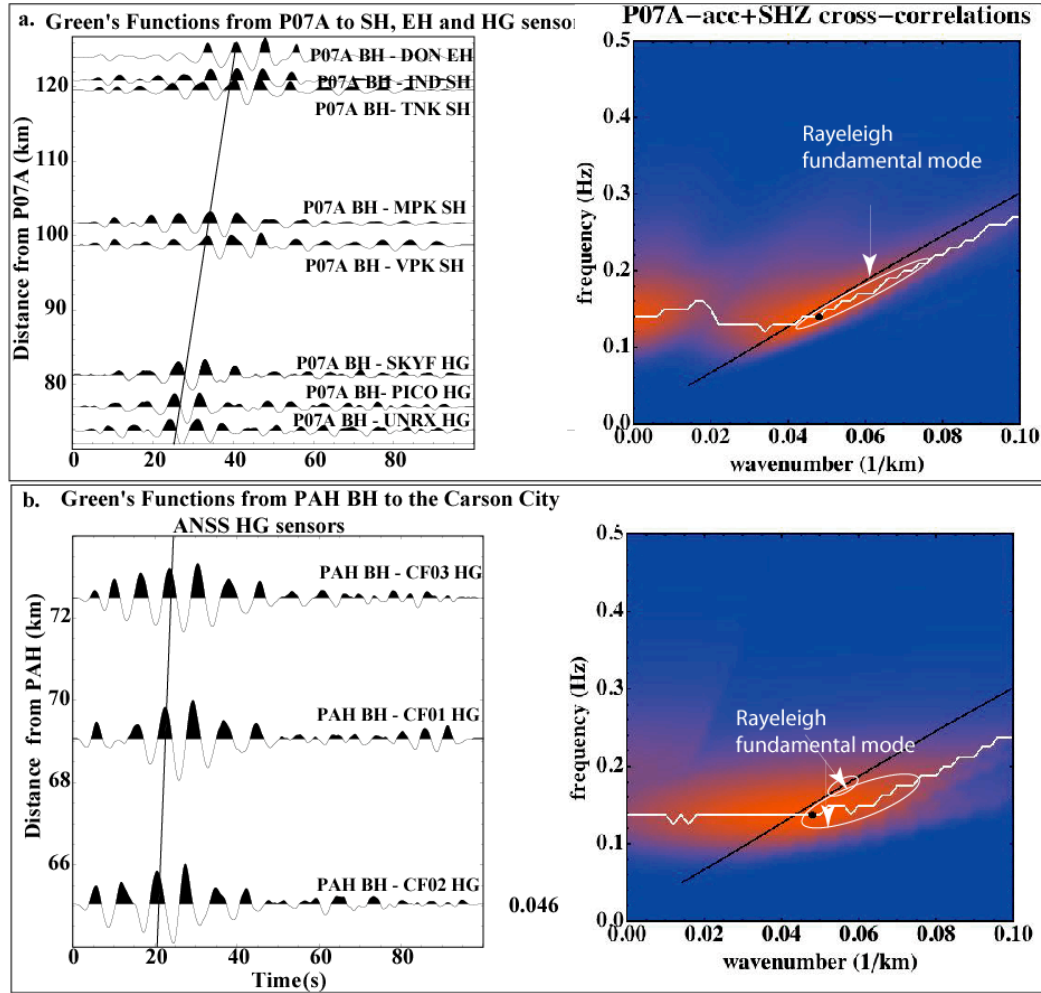


Figure 7. Shows retrieval of GF's from pairs BH and EH, SH, and HG sensors. Waveforms are filtered using a 0.1 - 1 Hz four-pole, zero-phase Butterworth filter. The left plots in each inset show GF record sections for pairs of stations including the P07A BH (Figure 7a) and PAH BH (Figure 7b). The right plots show GF FK analysis. Note lower Rayleigh phase velocity values in the Reno-Carson area when compared to the reference dispersion curve (black line) from Priestley and Brune (1978). The black line in the left plot shows the time lags for 3 km/s phases. The encircled areas on the FK plots show the range of values we use for phase velocity estimation. Note the absence of identifiable higher modes in both insets, unlike for the stations in Figure 6. The black dot marks the largest amplitude value in each FK plot. The white trace on the FK plots shows the maxim FK value for each wavelength.

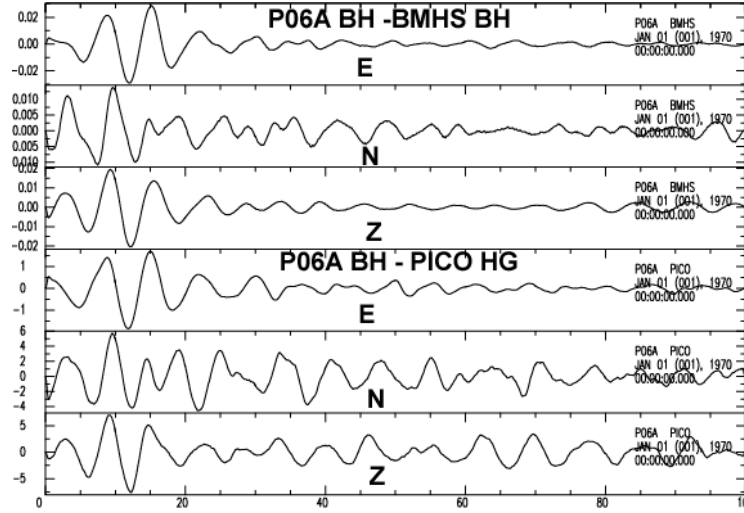


Figure 8. Similar shape GF's are extracted on all three components for the P06A BH - BMHS BH pair (upper three plots) and the P06A BH -PICO HG pair (lower three plots). The time length for stacking was two years.

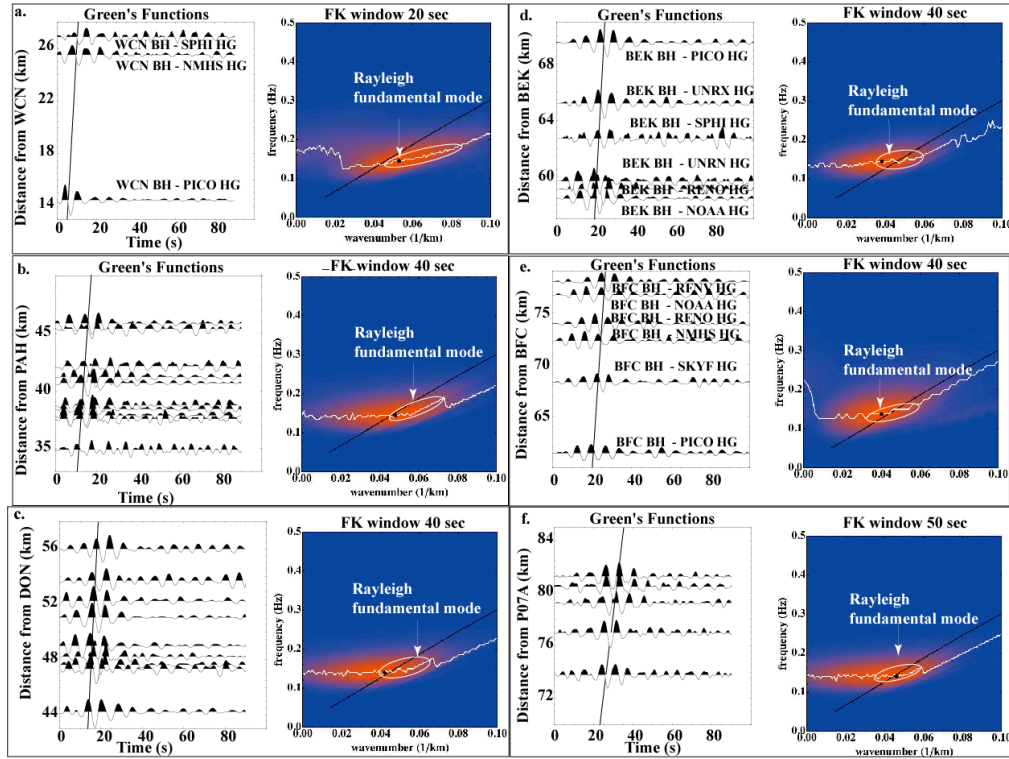


Figure 9. The phase velocity results beneath ad-hoc combinations of stations within the ANSS array in the Reno Basin extracted for paths from these stations and a station in the Reno-Carson area. Left plot in each inset shows the GF's we have used. The right plot shows the phase velocity estimated at each ad-hoc array. All waveforms, except the ones in Figure 11b, are filtered from 0.1 - 1 Hz, using a four-pole, zero - phase Butterworth filter. Note different GF frequency content, as a function of path length. The reference dispersion curve (black line) in the right plots of each inset is from Priestley and Brune (1978). The white trace on the FK plots shows the maxim FK value for each wavelength.

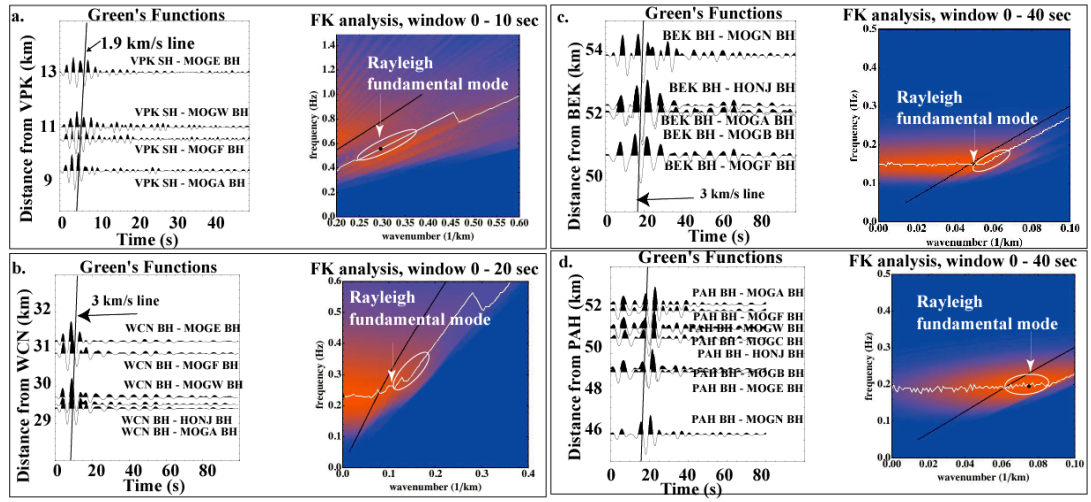


Figure 10. Examples of FK processing for phase velocity estimates beneath ad-hoc combinations of stations within the Mogul array, west of Reno, using paths from these stations and a station in the Reno-Carson area. The left plot in each inset shows the extracted GF's. The right plot shows the phase velocity estimated at each ad-hoc array. All waveforms are filtered from 0.1 - 1 Hz, using a four-pole, zero - phase Butterworth filter, except for the path between VPK and the Mogul array. The frequency band for this path is 0.5 - 1 Hz. For VPK, for GF extraction waveforms were crosscorrelated after a 0.5 Hz highpass Butterworth, zero-phase filter was applied. Note different GF frequency content, as a function of path length. The reference dispersion curve (black line) in the right plots of each inset is from Priestley and Brune (1978). The white trace on the FK plots shows the maxim FK value for each wavelength.

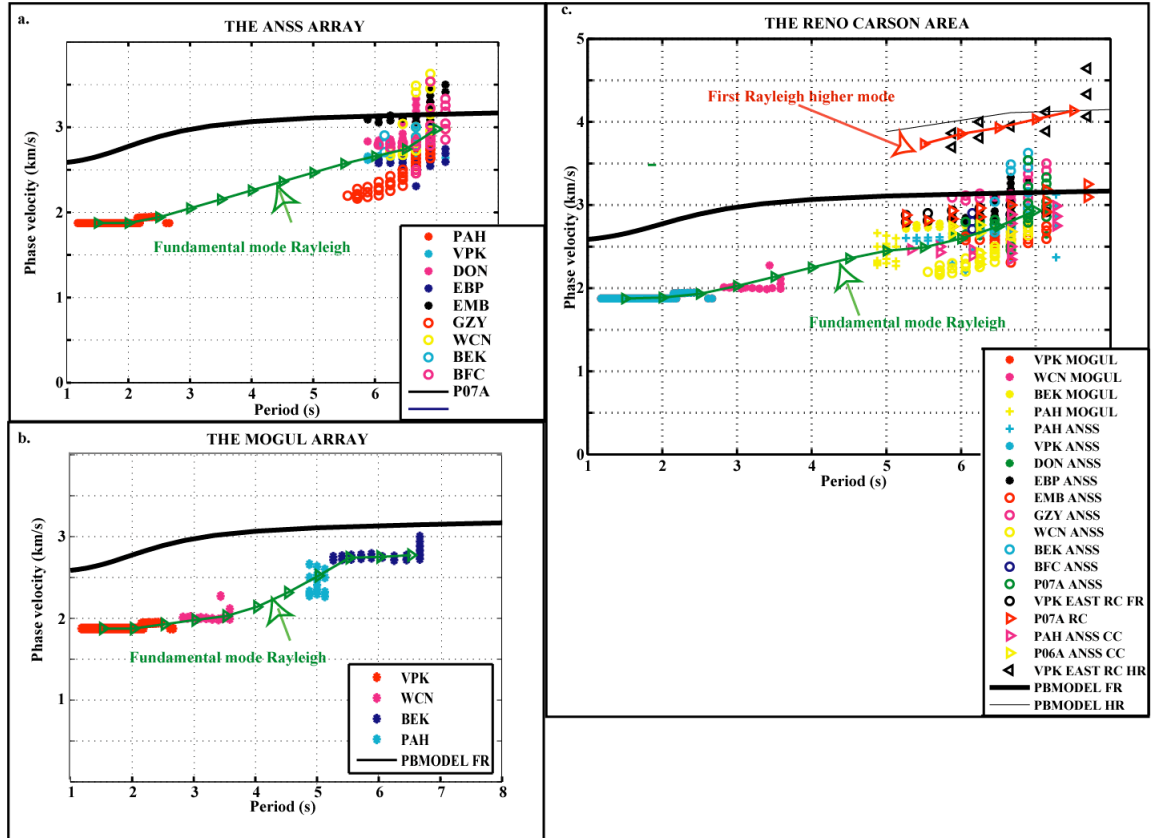


Figure 11 a) Phase velocity beneath the ANSS array in Reno, extracted from pairs of stations in Figure 9 and from pairs of stations not shown in Figure 9, however listed in Table 1; b) Phase velocity beneath the Mogul array extracted from pairs of stations in Figure 10; c) Phase velocity (see also Table 2) estimated for all the ad-hoc arrays in the Reno-Carson area. The arrays are shown in Figures 6,9,10 and in Table 1. The green triangles and the green line in each plot show the median value in 0.5 km/s bins of the fundamental Rayleigh (FR) phase velocity. The red line shows the values estimated the same way for the first Rayleigh higher mode (HR). Measurements at each "source" station are marked by symbols in the legend. The black curves in each plot show the phase velocity estimated using the Priesley and Brune (1978) model for FR (all plots-thick curves) and for first Rayleigh higher mode (HR) in plot c (thin black curve).

**Table 1.** Inter-station distance and station location for station pairs in Figures 3-10.

Station 1	Station 2	Distance (km)	Back Azimuth (deg)	Lat. Station 1 (deg)	Lon Station 1 (deg)	Lat. Station 2 (deg)	Lon. Station 2 (deg)
SMI	TNK	71.2	339	39.8673	-120.5295	39.2675	-120.2358
EMB	MMC	108.6	309	38.9748	-120.1019	38.3608	-119.1283
GNO	SMI	119.4	150	38.9292	-119.8528	39.8673	-120.5295
GZY	LUL	247.4	329	39.9620	-120.6502	38.0523	-119.1803
LUL	EBP	80.3	137	38.0523	-119.1803	38.5828	-119.8063
LUL	IND	181.3	147	38.0523	-119.1803	39.4343	-120.2917
Figure 6 a							
STRY	VPK	38.5	117	39.3151	-119.6386	39.4747	-120.0373
VPK	PICO	22.9	282	39.4747	-120.0373	39.4312	-119.7756
WAK	VPK	119.7	154	38.5044	-119.4372	39.4747	-120.0373
WCN	VPK	30.8	128	39.3017	-119.7563	39.4747	-120.0373

WIL	VPK	74.6	171	38.8104	-119.9083	39.4747	-120.0373
WVA	VPK	55.3	19	39.9445	-119.8240	39.4747	-120.0373
YER	VPK	87.6	128	38.9845	-119.2407	39.4747	-120.0373
Figure 6 b							
BEK	VPK	51.5	327.8	39.8667	-120.3586	39.4747	-120.0373
BFC	VPK	74.4	150.0	38.8940	-119.6077	39.4747	-120.0373
BMR	VPK	73.7	342.9	40.1087	-120.2910	39.4747	-120.0373
EUR	VPK	65.5	298.5	39.7542	-120.7108	39.4747	-120.0373
TNK	VPK	28.6	216.5	39.2675	-120.2358	39.4747	-120.0373
VPK	LOY	26.6	140.1	39.4747	-120.0373	39.6587	-120.2358
VPK	GZY	75.3	135.7	39.4747	-120.0373	39.9620	-120.6502
Figure 7 a							
P07A	PICO	77.0	80.6	39.5399	-118.8893	39.4312	-119.7756
P07A	SKYF	81.2	85.1	39.5399	-118.8893	39.4825	-119.8340
P07A	DON	124.6	79.8	39.5399	-118.8893	39.3517	-120.3205
P07A	IND	120.9	83.9	39.5399	-118.8893	39.4343	-120.2917
P07A	MPK	101.6	74.1	39.5399	-118.8893	39.2957	-120.0302
P07A	SKYF	81.2	85.1	39.5399	-118.8893	39.4825	-119.8340
P07A	TNK	119.5	74.9	39.5399	-118.8893	39.2675	-120.2358
P07A	UNRX	73.8	87.4	39.5399	-118.8893	39.5141	-119.7493
P07A	VPK	98.7	85.4	39.5399	-118.8893	39.4747	-120.0373
Figure 7b							
PAH	CF01	69.06277	28.1	39.7065	-119.3842	39.1593	-119.7647
PAH	CF02	65.05324	28.0	39.7065	-119.3842	39.1907	-119.7418
PAH	CF03	72.49207	26.8	39.7065	-119.3842	39.1257	-119.7676
Figure 8							
P06A	BMHS	30.3	157.7	39.6785	-119.8983	39.4257	-119.9764
P06A	PICO	29.4	158.9	39.6785	-119.8983	39.4312	-119.7756
Figure 9a							
WCN	NMHS	25.53751	176.31035	39.3017	-119.7563	39.5309	-119.7754
WCN	PICO	14.49437	173.42127	39.3017	-119.7563	39.4312	-119.7756
WCN	SPHI	26.89700	179.81671	39.3017	-119.7563	39.5436	-119.7573
Figure 9b							
PAH	HVGC	37.5	50.0	39.7065	-119.3842	39.4897	-119.7209
PAH	PICO	45.4	47.4	39.7065	-119.3842	39.4312	-119.7756
PAH	RENO	41.2	63.0	39.7065	-119.3842	39.5391	-119.8138
PAH	RFNV	40.7	68.6	39.7065	-119.3842	39.5742	-119.8275
PAH	SKYF	45.8	56.9	39.7065	-119.3842	39.4825	-119.8340
PAH	SMRN	34.9	57.2	39.7065	-119.3842	39.5372	-119.7274
PAH	UNRN	42.1	61.6	39.7065	-119.3842	39.527	-119.818
PAH	UNRX	37.8	55.5	39.7065	-119.3842	39.5141	-119.7493
PAH	NMHS	38.7	239.8	39.5309	-119.7754	39.7065	-119.3842
PAH	NOAA	38.4	246.5	39.5681	-119.7958	39.7065	-119.3842
Figure 9c							
DON	EGLV	56.0	292.7	39.3517	-120.3205	39.1580	-119.7196
DON	HVGC	53.7	253.6	39.3517	-120.3205	39.4897	-119.7209
DON	NOAA	51.0	242.0	39.3517	-120.3205	39.5681	-119.7958
DON	PICO	47.6	259.4	39.3517	-120.3205	39.4312	-119.7756
DON	RENO	48.2	244.5	39.3517	-120.3205	39.539	-119.8138
DON	RFNV	49.0	239.8	39.3517	-120.3205	39.5742	-119.8275
DON	SKYF	44.2	250.9	39.3517	-120.3205	39.4825	-119.8340
DON	UNRN	47.3	245.8	39.3517	-120.3205	39.527	-119.81
DON	UNRX	52.2	249.9	39.3517	-120.3205	39.5141	-119.7493
Figure9d							
BEK	NOAA	58.4	304.7	39.8667	-120.3586	39.5681	-119.7958
BEK	PICO	69.5	314.3	39.8667	-120.3586	39.4312	-119.7756
BEK	RENO	59.1	308.1	39.8667	-120.3586	39.5391	-119.8138
BEK	SPHI	62.7	305.1	39.8667	-120.3586	39.5436	-119.7573
BEK	UNRN	59.7	309.4	39.8667	-120.3586	39.527	-119.818
BEK	UNRX	65.2	307.1	39.8667	-120.3586	39.5141	-119.7493
Figure 9e							
BFC	PICO	61.4	166.3	38.8940	-119.6077	39.4312	-119.7756
BFC	RENO	73.8	166.0	38.8940	-119.6077	39.5391	-119.8138
BFC	RFNV	77.9	165.8	38.8940	-119.6077	39.5742	-119.8275
BFC	NMHS	72.2	168.4	38.8940	-119.6077	39.5309	-119.7754
BFC	NOAA	76.6	167.7	38.8940	-119.6077	39.5681	-119.7958

BFC	PICO	61.4	166.3	38.8940	-119.6077	39.4312	-119.7756
BFC	SKYF	68.2	163.3	38.8940	-119.6077	39.4825	-119.8340
Figure 11f							
P07A	EGLV	83.0	58.9	39.5399	-118.8893	39.1580	-119.7196
P07A	HVGC	71.5	85.2	39.5399	-118.8893	39.4897	-119.7209
P07A	NMHS	75.9	88.9	39.5399	-118.8893	39.5309	-119.7754
P07A	PICO	77.0	80.6	39.5399	-118.8893	39.4312	-119.7756
P07A	RENO	79.2	89.6	39.5399	-118.8893	39.5391	-119.8138
P07A	RFNV	80.5	92.4	39.5399	-118.8893	39.5742	-119.8275
P07A	SKYF	81.2	85.1	39.5399	-118.8893	39.4825	-119.8340
P07A	SMRN	71.8	89.4	39.5399	-118.8893	39.5372	-119.7274
P07A	SPHI	74.4	90.0	39.5399	-118.8893	39.5436	-119.7573
P07A	UNRX	73.8	87.4	39.5399	-118.8893	39.5141	-119.7493
Figure 10a							
MOGA	VPK	9.4		39.5222	-119.9454	39.4747	-120.0373
MOGE	VPK	13.1		39.5517	-119.9216	39.4747	-120.0373
MOGF	VPK	10.1		39.5362	-119.9492	39.4747	-120.0373
MOGW	VPK	10.6		39.5301	-119.9360	39.4747	-120.0373
Figure 10b							
WCN	HONJ	29.5	149.5	39.3017	-119.7563	39.5307	-119.9302
WCN	MOGA	29.4	146.4	39.3017	-119.7563	39.5222	-119.9454
WCN	MOGE	31.2	152.8	39.3017	-119.7563	39.5517	-119.9216
WCN	MOGF	30.8	147.5	39.3017	-119.7563	39.5362	-119.9492
WCN	MOGW	29.7	148.6	39.3017	-119.7563	39.5301	-119.9360
Figure 10c							
BEK	HONJ	52.3		39.8667	-120.3586	39.5307	-119.9302
BEK	MOGA	52.1	315.6	39.8667	-120.3586	39.5307	-119.9302
BEK	MOGB	52.1	317.4	39.8667	-120.3586	39.5222	-119.9454
BEK	MOGN	53.9	313.9	39.8667	-120.3586	39.5425	-119.9186
MOGF	BEK	50.7	311.2	39.8667	-120.3586	39.5481	-119.8836
Figure 10d							
PAH	HONJ	50.6	67.1	39.7065	-119.3842	39.5307	-119.9302
PAH	MOGA	52.2	66.7	39.7065	-119.3842	39.5222	-119.9454
PAH	MOGB	49.2	68.1	39.7065	-119.3842	39.5425	-119.9186
PAH	MOGC	51.1	67.0	39.7065	-119.3842	39.5285	-119.9348
PAH	MOGE	49.1	69.3	39.7065	-119.3842	39.5517	-119.9216
PAH	MOGF	51.9	68.4	39.7065	-119.3842	39.5362	-119.9492
PAH	MOGN	46.2	67.4	39.7065	-119.3842	39.5481	-119.8836
PAH	MOGW	51.1	67.2	39.7065	-119.3842	39.5301	-119.9360
Other groups of stations used in this study, and not illustrated in the figures, however used in Figure 11							
GZY	NMHS	88.8	302	39.9620	-120.6502	39.5309	-119.7754
GZY	NOAA	85.1	301	39.9620	-120.6502	39.5681	-119.7958
GZY	PICO	95.2	308	39.9620	-120.6502	39.4312	-119.7756
EMB	HVGC	65.9	209	38.9748	-120.1019	39.4897	-119.7209
EMB	NMHS	67.9	204	38.9748	-120.1019	39.53	-119.7754
EMB	NOAA	71.0	201	38.9748	-120.1019	39.5681	-119.7958
EMB	PICO	58.0	209	38.9748	-120.1019	39.4312	-119.7756
EMB	RENO	67.4	201	38.9748	-120.1019	39.5391	-119.8138
SPHI	EMB	69.8	25	39.5436	-119.7573	38.9748	-120.1019
EBP	HVGC	101.1	184	38.5828	-119.8063	39.489	-119.7209
EBP	NMHS	105.4	181	38.5828	-119.8063	39.530	-119.7754
EBP	NOAA	109.5	180	38.5828	-119.8063	39.568	-119.7958
EBP	PICO	94.3	181	38.5828	-119.8063	39.4312	-119.7756
EBP	RENO	106.3	179	38.5828	-119.8063	39.539	-119.8138
EBP	RFNV	110.2	179	38.5828	-119.8063	39.5742	-119.8275
EBP	SKYF	100.0	178	38.5828	-119.8063	39.4825	-119.8340
EBP	UNRX	103.6	182	38.5828	-119.8063	39.514	-119.7493
BAB	NOAA	26.7	97	39.60	-120.104	39.56	-119.79
BAB	PICO	33.9	123	39.6013	-120.1040	39.431	-119.7756
BAB	RENO	25.87	105	39.6013	-120.10	39.53	-119.81
BAB	UNRX	31.98	107	39.60	-120.10	39.51	-119.7493

UNRN	YER	78.1	320.6	39.527	-119.818	38.9845	-119.2407
YER	NOAA	80.5	143	38.9845	-119.2407	39.5681	-119.7958
YER	PICO	67.7	136	38.9845	-119.2407	39.4312	-119.7756
YER	RENO	78.9	141	38.9845	-119.2407	39.5391	-119.8138
YER	RFNV	82.7	142	38.9845	-119.2407	39.5742	-119.8275
WVA	HVGC	51.3	350	39.9445	-119.8240	39.489	-119.7209
WVA	RENO	45.0	358	39.9445	-119.8240	39.53	-119.8138
WVA	RFNV	41.1	0.4	39.9445	-119.8240	39.5742	-119.827
WVA	SKYF	51.3	0.9	39.9445	-119.8240	39.4825	-119.8340
WVA	UNRX	48.2	352	39.9445	-119.8240	39.51	-119.7493
EMB	HVGC	65.9	209	38.9748	-120.1019	39.4897	-119.7209

**Table 2. Phase velocity dispersion curves extracted in Figure 11**

MOGUL		ANSS RENO		RENO-CARSON AREA			
				Rayleigh Fundamental mode		Rayleigh first higher mode	
Period (s)	Phase velocity (km/s)	Period (s)	Phase velocity (km/s)	Period (s)	Phase velocity (km/s)	Period (s)	Phase velocity (km/s)
1.5	1.87	1.5	1.87	1.5	1.87	5.5	3.73
2.0	1.87	2.0	1.87	2.0	1.89	6.0	3.85
2.5	1.93	2.5	1.94	2.5	1.93	6.5	3.93
3.0	1.98	3.0	2.05	3.0	2.02	7	4.03
3.5	2.03	3.5	2.15	3.5	2.13	7.5	4.13
4.0	2.14	4.0	2.25	4.0	2.25		
4.5	2.32	4.5	2.36	4.5	2.36		
5.0	2.52	5.0	2.47	5.0	2.47		
5.5	2.74	5.5	2.57	5.5	2.59		
6.0	2.75	6.0	2.66	6.0	2.65		
6.5	2.77	6.5	2.74	6.5	2.74		
		7.0	2.98	7.0	2.93		

**Table 3. Shear velocity models extracted from the dispersion curves in Table 2 and Figure 11.**

Location	Mogul array	ANSS array	Reno-Carson area	Starting model ANSS and Mogul	Starting model Reno-Carson area
Layer thickness (km)	Shear velocity (km/s)	Shear velocity (km/s)	Shear velocity (km/s)	Shear velocity (km/s)	Shear velocity (km/s)
1	1.6	1.7	1.7	0.8	1.0
1	2.4	2.5	1.7	1.7	1.7

2	2.5	2.6	2.2	2.1	2.1
2	2.5	2.7	2.7	2.6	2.6
2	3.6	3.7	3.8	2.8	2.8